

Reflectance Anisotropy of Trees in ADS40 Line-Sensor Images

Implications for Species Classification in Finland

Felix Rohrbach, ETH Zürich

Master Thesis 2010



Eidgenössische Technische Hochschule Zürich
Swiss Federal Institute of Technology Zurich



HELSINGIN YLIOPISTO
HELSINGFORS UNIVERSITET
UNIVERSITY OF HELSINKI

Reflectance Anisotropy of Trees in ADS40 Line-Sensor Images - Implications for Species Classification in Finland

Master Thesis for MSc ETH in Geomatics Engineering and Planning

Spring Semester 2010

Author:

Felix Rohrbach
Hohrainlistrasse 19
8302 Kloten
felix@rohrba.ch
+41 79 776 4947

Supervisors:

Prof. Dr. Hilmar Ingensand
Institute of Geodesy and Photogrammetry, ETH Zürich
hilmar.ingensand@geod.baug.ethz.ch

Dr. Ilkka Korpela
Faculty of Agriculture and Forestry, University of Helsinki
ilkka.korpela@helsinki.fi

ETH Zürich
Institute of Geodesy and Photogrammetry
Chair for Photogrammetry and Remote Sensing
Wolfgang-Pauli-Str. 15
CH - 8093 Zürich

Abstract

In Finland, information about the species of a tree is valuable. Therefore research has been looking for an automated approach to retrieve such data by using remote sensing. While LiDAR had its breakthrough a few years ago, a recently introduced innovation brought new attention to passive optical sensors. With its absolutely calibrated sensor head, the ADS40 could be able to improve classification results by applying an atmospheric correction to the image data, thus changing the detected at-sensor radiances into at-target reflectances. With its high-resolution capability, the camera also enables intracrown analysis. Combining these features together with a LiDAR data set, Korpela et al. (2010) generated a unique data set, containing not only spectral features, but also geometric information for 121 crown points in over 16'000 trees. Even more, this data was extended with detailed tree-specific information, measured over several years by many students, teachers, and research assistants at the University of Helsinki. Although the amount data reduced by limiting to trees of the three main species and which were in a healthy condition, the used set contained an impressive number of 15'197 trees.

In this master thesis, the effect of the atmospheric correction was tested in a forest area. It was shown, that after applying the algorithm, dependencies for the view zenith angle (VZ) decreased for sun-lit points. For the resulting reflectance values, the R^2 -value was reduced up to 16% in the blue band. Even though the back-lit sides of trees already had negative trends, the correction method dampened these further. This showed, that a separation between these two illumination cases is needed for either the atmospheric correction, or when later classifying the data.

While VZ showed to have a linear behaviour for reflectances, the view azimuth angle (VA) was better fitting to a simple non-linear model. Even though for the sun-lit side the quadratic curve almost matched the linear regression, the shaded part of the crown showed to separate more clearly. Differences between the R^2 -values of both regression models reached a maximum of 5.5% for pines in the blue band.

To conclude this thesis, an analysis of the whole crown was done as last experiment. While on the sun-lit side, points achieved a relative mean reflectance of 79.4%–153.1% compared to the top, the self-shaded part only reached values from 42.8% to 112.8%. The best defined crown points (lowest standard deviation) were in the direction to the sun, or in the exact opposite, at an offset angle of 180°.

The overview of all the 121 crown points nicely visualises the different behaviour for each tree species. Unfortunately, this indicates that a single model for correcting the reflectance anisotropy in trees might not be enough. On the other hand, further research will show, if these differences could be used to determine the tree species using reflectance observations.

Acknowledgements

Even though this thesis was conducted at the Institute of Geodesy and Photogrammetry at the Swiss Federal Institute of Technology (ETH) in Zürich, it was supervised by Dr. Ilkka Korpela from the University of Helsinki. I would like to thank him for making this thesis possible and as well for his advice and guidance during this work. To collaborate over such a distance is always a special challenge, which was mastered successfully in our case. I am also thankful to Prof. Dr. Hilmar Ingensand for accepting this topic for my final thesis during my studies.

I want to thank my dearest friends and fellow sufferer from the HIL C62.1 at ETH Hönggerberg. While litres of coffee gave me the energy required, they provided me with the social company, which kept me motivated. A special mention earned soon-to-be-Dr David Novák. Always available for discussions, he even offered a personal 24/7 emergency hotline, thus being always there for all of us, whenever we needed his support and technical advice.

Above all, I want to thank my family and my girlfriend. Thank you for encouraging me during my studies. Having such support really was the backbone of this thesis.

The underlying data could only be realised thanks to several people, who should be thanked at this place. The reference data used in this thesis was measured over the years by many students, teachers, and research assistants at the University of Helsinki, to whom I express my gratitude. The ADS40 test flight in 2008 was made possible by Jorma Kivinen, Peep Krusberg, Risto Kuittinen, Kai Lämmer, Heikki Luukkonen, Lasse Rahkonen, and Arthur Rohrbach. Data post processing was done by Fernando Schapira, Jonne Davidsson, Lauri Markelin, Yuji Kuwano, while Jyrki Lämsä, Harri Kaartinen, Pekka Savolainen, and Seppo Tötterström helped with GPS and geodetic transformations. Udo Tempelmann and Tauno Saks assisted in sensor modelling and with the XPro software. Funding to acquire the data was made available by Metsähallitus, University of Helsinki, Suomen Luonnonvarain Tutkimussäätiä, Academy of Finland (High Resolution Remote Sensing Potential to Measure Single Trees and Site Quality, no. 123193), and the Ministry of Agriculture and Forestry.



Zürich, 5 July 2010

Felix Rohrbach

Table of Contents

Abstract.....	I
Acknowledgements	II
Table of Contents.....	III
Notations	IV
Abbreviations.....	V
1 Introduction	1
2 Background	4
2.1 Geometry of passive optical imaging	4
2.2 On the radiometry of passive optical sensing	4
2.3 The ADS40 sensor and XPro software	6
2.4 Earlier studies in forest reflectance anisotropy and image-based tree species recognition	8
3 Material and Methods	10
3.1 Study area and reference trees.....	10
3.2 ADS40-SH52 image data	11
3.3 Image processing and acquisition of image features for the reference trees.....	13
3.3.1 Image Postprocessing (ORIMA and XPro work)	13
3.3.2 Visibility check for the reference trees	13
3.3.3 Crown modelling	15
3.3.4 Crown sampling	16
3.4 View illumination geometry.....	18
3.5 Analysis of the success of the ATM correction using trees as reflectance targets	21
3.6 Effect of changes in the view-direction.....	21
3.7 Trends in vertical and horizontal direction	22
3.8 Statistical methods.....	22
4 Results of experiments.....	23
4.1 Evaluation of ATM correction with trees	23
4.2 Influence of view azimuth direction.....	27
4.3 Intracrown variation	29
5 Discussion and Conclusions.....	33
6 References	36

Notations

σ	Standard deviation
ρ	Reflectance
$\bar{\rho}$	Reflectance of the surrounding area
Φ	Radiant flux [$\text{J}\cdot\text{s}^{-1}$]
c_1	Sensor-line-specific calibration factor
d	Distance tree to camera [m]
df	Density factor
E	Irradiance [$\text{W}\cdot\text{m}^{-2}$]
h	Height of tree [m]
H	Flying altitude [m]
$h_{\text{Rel}1}, h_{\text{Rel}2}, h_{\text{Rel}3}$	Relative height compared to the maximum tree height in a 5-m, 10-m, 20-m circle
L	Radiance [$\text{W}\cdot\text{sr}^{-1}\cdot\text{m}^{-2}$]
L_0	Path radiance at zero ground reflectance [$\text{W}\cdot\text{sr}^{-1}\cdot\text{m}^{-2}$]
$p\text{Angle}$	Point angle = offset to SA [°]
Q	Radiant energy [J]
r	XY distance from LiDAR point to trunk [m]
R^2	Coefficient of determination
SA	Sun azimuth angle [°]
SZ	Sun zenith angle [°]
s	Atmospheric albedo
S	Mean solar spectral irradiance [$\text{W}\cdot\text{m}^{-2}$]
SS_{err}	Regression sum of squares
SS_{total}	Total sum of squares
t	Integration time [s]
T_{down}	Downwards transmittance of the atmosphere
T_{up}	Upwards transmittance of the atmosphere
VA	View azimuth angle [°]
VZ	View zenith angle [°]
w	Crown width [m]
x_{rel}	Relative offset from the top

Abbreviations

ASR	At-sensor-radiance (image version)
AT	Aero triangulation
ATM	Atmospherically corrected (image version)
B16A	Backwards looking view in ADS40-SH52
BLU	Blue band
BRDF	Bidirectional reflectance distribution function
BS	Both-shaded illumination class (by neighbour and tree itself)
CIR	Colour-Infrared (image)
DBH	Diameter-at-breast-height
DN	Digital number, grey value of the pixel
DPW	Digital Photogrammetric Workstation
DST	Daylight saving time
EO	Exterior orientation
FWHM	Full width at half maximum
GMT	Greenwich mean time
GPS	Global Positioning System
GRN	Green band
GSD	Ground sample distance
IFOV	Instantaneous field of view
IMU	Inertial measurement unit
L0	Raw version of the ADS image data
L1	Rectified (epipolar) version of the ADS image data, can be ASR, ATM, or BRDF corrected
LiDAR	Light Detection and Ranging
N00A	Nadir looking view
NDVI	Normalised Difference Vegetation Index calculated using RED and NIR: $(\text{NIR}-\text{RED})/(\text{NIR}+\text{RED})$
NIR	Near-infrared band
OS	Other-shaded illumination class (by neighbour)
PAN	Panchromatic (band)
R ²	Coefficient of determination
RED	Red band
RGBN	A combination of channels red, green, blue and near-infrared
RMSE	Root mean square error
RSE	Residual standard error
RTK	Real Time Kinematic
SA	Sun azimuth angle
SI	International System of Units
SL	Sun-lit illumination class
SS	Self-shaded illumination class (by tree itself)
SZ	Sun zenith angle
VA	View azimuth angle
VRS	Virtual Reference Station
VZ	View zenith angle

1 Introduction

At first sight, the automated task of tree species classification in Finland seems to be straightforward, since 97% of the stem volume constitutes of either pine (*Pinus sylvestris* L.), spruce (*Picea abies* (L.) H. Karst), or birch (*Betula pubescens* Ehrh. and *Betula pendula* Roth.) (Tomppo et al., 2001). But photogrammetric attempts during the last 30 years have shown that the forest canopy conceals various challenges when using passive optical remote sensing.

Knowledge of the tree species is crucial to Scandinavian foresters for ecological (forest management, forest protection), economic (timber value) and technical (wood procurement logistics) reasons, and therefore an efficient way of collecting such data is of great interest. Korpela and Tokola (2006) suggested that the species classification accuracy for the main species should reach at least 95% to be adequate. Using visual interpretation of large-scale colour-infrared (CIR) images, this limit was achieved in Finland (Korpela, 2007). These results gave a baseline for the development of automatic methods.

Sensor Fusion

Parallel to the change from analogue to digital remote sensing, the introduction of airborne LiDAR was a breakthrough (Næsset, 1997, 2002; Hyypä and Inkinen, 1999; Hyypä et al., 2008). The question of combining the advantages of both technologies soon emerged. For both, the estimation of parameters for trees as well as forest areas, image data is regarded as a complement to LiDAR, above all for the species recognition sub-task (e.g. Leckie et al., 2003). However, the use of two sensors increases risks, complexity, and costs. Nevertheless, the capability of aerial imagery to separate birch from pines and spruce using the near-infrared band, is considered to improve the classification accuracy of LiDAR.

Modelling the Atmosphere

When working with remote sensing data, the effect of the atmosphere transmittance has been shown to be significant and heavily dependent on the solar- and view geometry as well as the flight altitude on which the data was collected (Beisl et al., 2008). The removal of this disturbance has been a field of research for itself, and many attempts have been made to correctly model the medium between the camera and the target (e.g. Chavez, 1988; Fraser et al., 1992; Kaufman and Sendra, 1988). In version 4.2 of their photogrammetric software XPro, Leica Geosystems added the option of creating atmospherically corrected images (Beisl and Woodhouse, 2008). This function constitutes the end of a complete radiometric processing chain, which starts with the calibration of the sensor during manufacturing. Since the sensor head is not only calibrated relatively between values on the focal plane, but to absolute values using an integrating light sphere, the digital numbers in an image not only represent a grey value, but also a measurement in physical SI-units. Having this connection to measurable attributes enabled the application of a model, which corrects for the atmospheric influence, resulting in observations describing the reflectance ρ of a target area.

Reflectance Anisotropy in Aerial Images

While the measurement of reflectance anisotropy has been feasible for well-defined surfaces on the ground, the corresponding instrument for examining the reflectance of trees has not existed until now. Li and Strahler (1986) showed, that the reflectance anisotropy of forest scenes is largely

explained by the illumination and viewing geometry, which is displayed for a vertical frame sensor image in Figure 1.

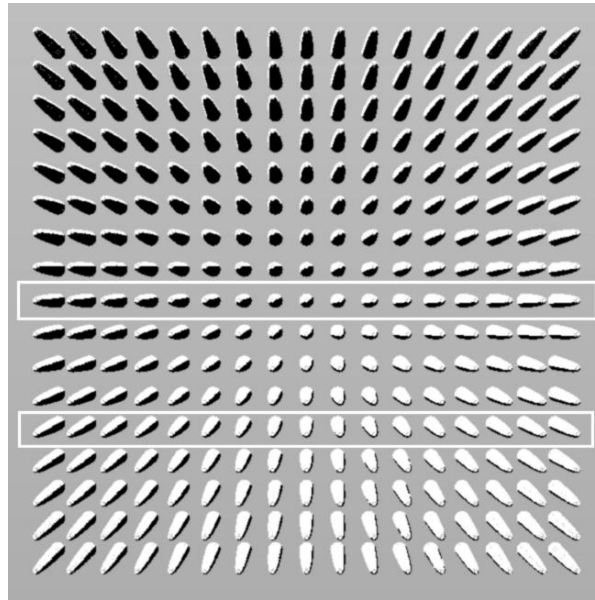


Figure 1: Trees as seen in a perspective view. The azimuth of the sun is approximately 340° . The white rectangles depict the 1-dimensional view-illumination geometry that is achieved by a line sensor having a nadir-looking CCD-line and a backwards looking CCD-line. (Korpela et al., 2010)

As Leica Geosystems ADS40 is a digital pushbroom camera, the viewing geometry is already simplified for the recorded image. The alignment of the multispectral (RGBN) sensor lines on the focal plane results in only two viewing angles, nadir at 0° (N00A) and backwards at 16° (B16A). Using this camera allows, for the first time in photogrammetric data, to study the reflectance anisotropy of forest trees, to examine if this property can be used for tree species classification and if the use of a calibrated line sensor, where the anisotropy effects are reduced (Figure 1), is more efficient for the species classification task.

Combining Image and LiDAR Data

For the analysis of the tree crown itself, a link between the geometric object and the image has to be established. Although the ADS40 stores all the orientation parameters for each line recorded by the sensor, a second perspective or a surface model is required to reconstruct the position of each pixel in the 3D object space. If both, the N00A and B16A view are activated, the generation of a forest canopy height model would technically be possible using image matching algorithms. However, for this data set, the available LiDAR points will be used to create crown envelopes. These surface models will then be used to acquire additional geometric information for the tree crown.

Objectives

Objectives of this thesis are

- To examine the dependencies of the spectral signatures of different main tree species of Finland in the varying view-illumination geometry in order to find robust invariant spectral features for species classification
- To examine the intracrown reflectance anisotropy and reflectance observations in varying illumination conditions (direct, diffuse light)

More specifically, I analysed following questions within the scope of this master thesis:

1. How is the atmospheric correction affecting the reflectance anisotropy in trees?
2. Are the observed reflectances differing, when viewed from different directions?
3. Is the intracrown variation of reflectances similar for differing tree species?

Always considering the errors contained in the data and multicollinearities between variables that can easily lead to wrong conclusions and explanations.

In the following section 2, “Background”, information about passive optical imaging and its radiometric issues are given. The airborne digital sensor ADS40 and its capabilities for remote sensing applications are described as well as earlier studies in image-based tree species recognition and reflectance anisotropy of forest canopies are discussed.

Section 3, “Material and Methods”, describes the material (reference trees and camera configuration) used in the study. It contains an overview of the applied postprocessing steps, the experiments made, and the statistical methods used.

Section 4 presents the results of the study, which are then discussed in the final concluding section.

2 Background

2.1 Geometry of passive optical imaging

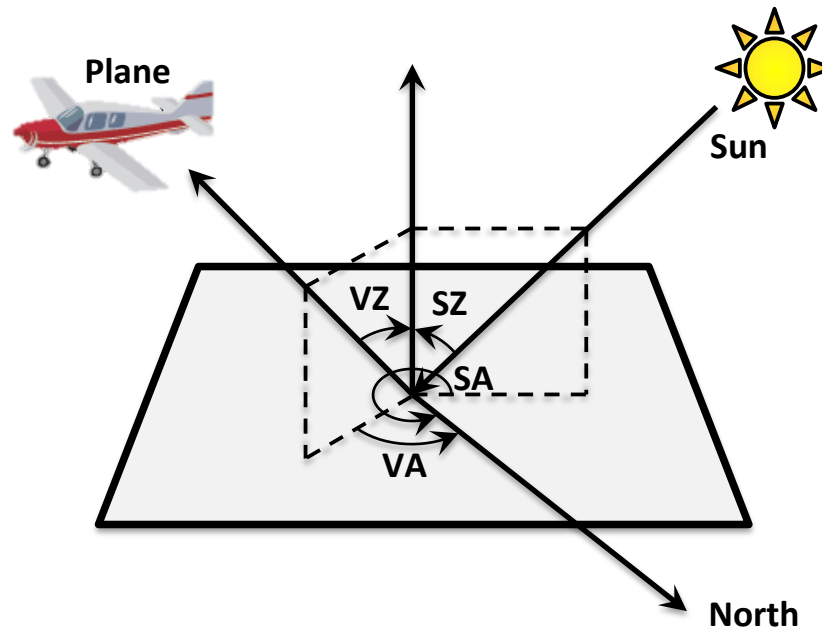


Figure 2: Observation geometry. The symbols are explained in the body text.

The observation geometry for remote sensing usually gets described using the four angles shown in Figure 2. The sun zenith (SZ) angle is the angle between the local surface normal and the vector pointing to the sun from the observed target. Correspondingly, the view zenith (VZ) angle describes the angle between the local surface normal and the vector pointing to the observer, in our case the camera.

Due to Finland's geographic location (60°N–67°N commercial forests), the SZ angle is generally very high (>37°). This leads to the problem that only the tops of the tallest, dominant trees can be observed in direct light and that these tall trees also cast a long shadow on their neighbours. Also, the photographic season and days are short.

The sun azimuth (SA) angle is the angle between the north direction and the projection to the ground of the vector pointing towards the sun. Similarly, the view azimuth (VA) angle is the angle between the north direction and the projection to the ground of the vector pointing towards the camera. If the difference of SA and VA is small, the target is front-lit or in the backscatter geometry. Equally, a 180-degree difference implies back-lit (forward scattering) geometry.

As trees were located on both sides of the plane for certain flight lines (0833, 0843, 0852) a signed view zenith angle (SVZ) is introduced. While trees on the right hand side of the flying direction remain the same as for VZ, for angles towards the left a negative sign is applied.

2.2 On the radiometry of passive optical sensing

The interaction of light with the atmosphere and also its reflection properties on different surfaces are challenging fields of research. Starting from the definition of terms for physical quantities and effects, up to modelling and correcting for unknown influences. Schaepman-Strub et al. (2006) presented an overview of the most used terms and also showed how they are often misused. For this

thesis, only the basic units are explained, following the definitions found in Albertz and Wiggenhagen (2009).

Radiant flux	Φ	$[\text{J}\cdot\text{s}^{-1}]$	The radiant flux Φ is the radiant energy Q passing through an area per unit time.
Radiance	L	$[\text{W}\cdot\text{sr}^{-1}\cdot\text{m}^{-2}]$	The radiance L is the radiant flux per unit solid angle emitted per unit area.
Irradiance	E	$[\text{W}\cdot\text{m}^{-2}]$	The irradiance E is the radiant flux received per unit area.
Reflectance	ρ		The Reflectance ρ is the ratio of radiant flux, reflected by a body to that incident upon it.

Table 1: Definitions of radiometric quantities

Figure 3 shows the main radiation components reaching the sensor. The illumination of the target consists of the direct sun light (A) and the scattered light from the sky hemisphere (B), which also contributes considerably, compared to the second order scattered light (D), which usually can be neglected. Additionally surrounding objects (i.e. neighbouring higher trees) influence the illumination by either shadowing or enlightening the area, depending on their own reflectance and the brightness of the target (F). This should not be underestimated. Multiple scattering by trees contributes to the total radiance towards the sensor and Nilsson and Peterson (1991) estimated it to be 9% in the RED band, while increasing up to 45% in the NIR band.

In addition to the direct reflected light (G), the path radiance (C) and the scattered light from the surrounding area (E) contribute to the radiance measured at the sensor.

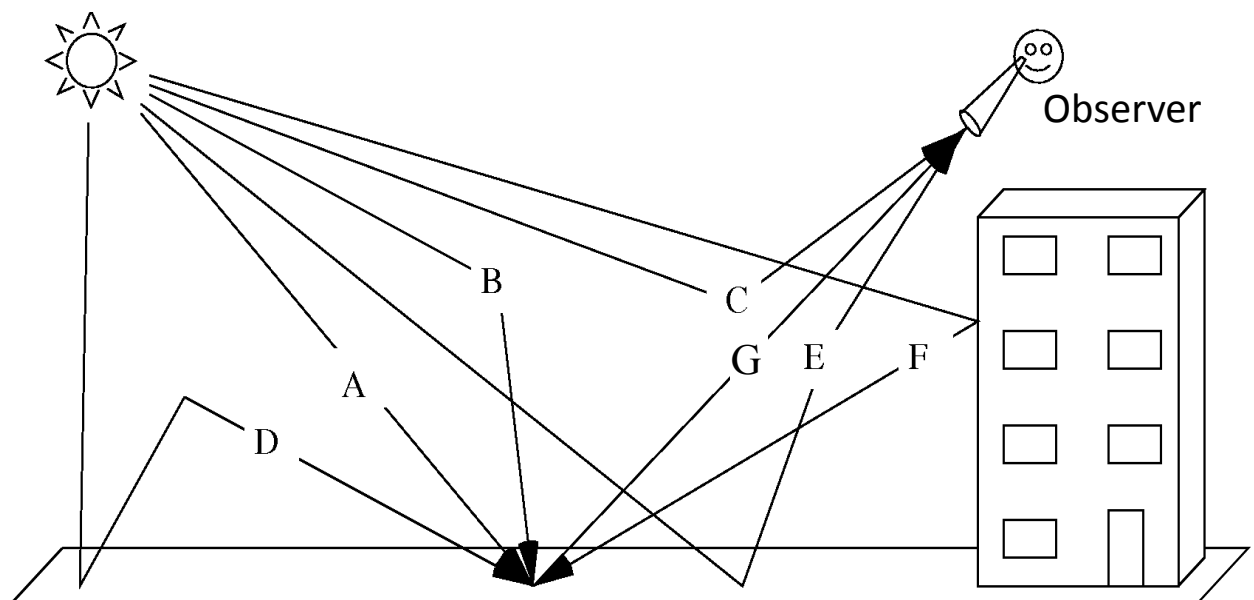


Figure 3: Radiation components reaching the sensor in the reflective wavelength range (400 nm – 2500 nm) (Beisl and Woodhouse, 2008)

Schaepman-Strub et al. (2006) also point out, that since there are no unlimited small light sources, and therefore no unlimited small sensor IFOVs, the reflected light (G) is not really directional, but more to be treated as conical. But as for many radiometrical models and this study, this effect will be neglected.

2.3 The ADS40 sensor and XPro software

The ADS40 is a high-resolution digital airborne camera using the pushbroom (3-line) design known from various remote sensing satellites. The first generation was developed in 2000 in a co-operation between DLR (German Aerospace Centre) and Leica Geosystems (LH-Systems at this time) to fulfil both photogrammetric (geometric) and remote sensing (radiometric) requirements. In late 2006 the second-generation ADS40 camera was introduced. First tests of this new version (ADS40-SH52, which was used in the experiments here) showed that the geometric accuracy of a block, taken at a flying altitude of 2000 metres, was within subpixel range using direct georeferencing alone. Using aerial triangulation and self-calibration, the RMSE improved to values between 0.18 and 0.31 of the ground sample distance (GSD, in this case 20cm) (Casella et al., 2008).

The second generation ADS40 exists with two different sensor head configurations. The difference is in the configuration of the focal plane. While the SH51 uses 8 sensor lines (PAN forward, RGBN & 2xPAN (staggered) nadir, and PAN backward) the more common SH52 comprises 12 sensor lines (PAN forward, RGBN & 2xPAN (staggered) nadir, RGBN & PAN backward) (Fricker, 2007). Each sensor line consists of 12'000, 6.5-micron pixels ($f = 62.7$ mm) allowing for taking nadir and backward 4-color images. Tetrachroids split the incoming light and project it to the corresponding sensor lines and the resulting bands are narrow, 50 nm (Full width at half maximum, FWHM). Using this technology, the ADS40 is capable of recording co-registered, equal-resolution colour imagery.

Even though the camera enables stereo viewing in RGBN, providing image mats with almost 100% overlap, this feature (simultaneous use of the nadir and backward looking data) was not used in this thesis.

The quality of an image, and also its value for remote sensing applications, depends not only on the camera, but on the whole image acquisition chain. Starting from the camera, which needs to be calibrated, continuing through a medium (atmosphere, clouds, fog), which needs to be modelled correctly, up to the proper post processing. At the moment, the ADS40 (in combination with the XPro software package) is the only digital airborne camera, which takes care of all the different parts of this image chain. For the Z/I Imaging DMC (version 2) camera absolute calibration was recently announced, which is a needed step for reflectance calibration. It is a frame sensor and in it, the calibration is solved for each shutter time and aperture stop-combination.

Radiometric Calibration

The ADS40 is factory calibrated using an integration sphere, which produces a homogenous light. For each sensor line, a calibration coefficient is determined, which is stored in the camera specific calibration file.

The emitted radiance L is known for the spectral band widths of the ADS40. This value is then compared to the pixel value (DN), which was measured by the camera during the calibration. Also taking account for the chosen integration time t , the sensor-line-specific calibration factor c_1 can then be calculated [1].

$$c_1 = L \cdot t / DN \quad [1]$$

Atmospheric Corrections in XPro

To correct for the atmospheric influences, Leica Geosystems developed and implemented a radiometric workflow for the ADS40 data, which also includes atmospheric correction algorithms and

an empirical BRDF correction (Beisl 2006; Beisl et al., 2008). The atmospheric correction which was applied for this data is based on the radiation transfer equation by Fraser et al. (1992), who described the radiance at the sensor using the following equation:

$$L_m = L_0 + \frac{\rho * S * T_{down} * T_{up}}{\pi * (1 - s * \bar{\rho})} \quad [2]$$

Where L_m = measured at-sensor radiance [$W \cdot sr^{-1} \cdot m^{-2}$]
 L_0 = path radiance for zero surface reflectance [$W \cdot sr^{-1} \cdot m^{-2}$]
 ρ = surface reflectance (0–1)
 $\bar{\rho}$ = average reflectance of surrounding area
 S = mean solar spectral irradiance [$W \cdot m^{-2}$]
 T_{down} = total downward transmittance (0–1) from top of the atmosphere to the ground
 T_{up} = total upward transmittance from ground to sensor
 s = spherical albedo of the atmosphere, i.e. the fraction of the upward radiance which is backscattered by the atmosphere

Two different multispectral image sets (RED, GRN, BLU, and NIR) were produced using Leica XPro (Version 4.2, Leica Geosystems AG, Heerbrugg, Switzerland) for both, the nadir (N00A) and backwards (B16A) view:

- At-sensor radiance image data (Product “calibrated” in the Software): ASR
- Atmospherically corrected target reflectance data (Product “atmospheric”): ATM

For the parameters, which are required for calculating the atmospheric correction, the default software settings were used for processing.

At-sensor radiance image data (ASR)

The ASR describes the radiance received by the camera, which is obtained using the specific calibration factor (and the integration time) determined during the camera calibration. The value is stored in an unsigned 16 bit range.

Using the same equation as applied during the calibration, but this time using the measured radiance (DN) instead of the known radiance by the sphere, the equation changes to:

$$L_m = DN * 50 * c_1 / t \quad [3]$$

In [3] L_m is the calibrated ASR pixel value, which is scaled in the image data to use the entire unsigned 16-bit range, using a factor of 50. This has to be remembered when working with at-sensor radiances.

Atmospherically corrected target reflectance data (ATM)

The atmospheric correction used for the ATM version of the images, is based on the equation by Fraser et al. (1992), shown in equation [2]. Not only attending to the different transmittances (T_{down} , T_{up}), which reduce the illumination on the path from the top of the atmosphere to the target and then to the camera, but also using the path radiance at zero ground reflectance L_0 . The illumination is enhanced by the multiple scattering between the surrounding area (with reflectance $\bar{\rho}$) and the atmospheric albedo s .

While some of the factors are known or measured, L_0 , T_{down} , T_{up} , and s are modelled (empirically) following Song et al. (2003).

As with the ASR data, the reflectance values (0–1) are multiplied by a factor of 10000 to make use of the entire unsigned 16 bit range, in which the pixels of the images are stored.

This method has been verified with a set of ADS40 calibration flights over the same target with different visibilities. In-situ ground reflectance measurements of different targets were made. The ADS40 reflectance values were found to be in good agreement with the measured ones (Markelin et al., 2010).

In addition to the four bands of the camera, the well-known normalized difference vegetation index (NDVI) was calculated using the RED and NIR band as shown in [4].

$$NDVI = \frac{NIR - RED}{NIR + RED} \quad [4]$$

Studies have indicated that reflectance anisotropy, which might be amplified by atmospheric effects in aerial imagery, could provide additional information specifically for species classification (Deering et al., 1999; Sandmeier and Deering, 1999; Walthall, 1997). For this thesis though, it is assumed that the influence of the medium between the camera and target is obtrusive, and that by applying an atmospheric correction, the remaining differences in spectra are only due to effects caused by reflectance anisotropy in the tree crowns themselves.

As these effects are usually depending on the view geometry, the ADS40 already simplifies the problem with its camera design. Limiting to two viewing angles (N00A and B16A) may facilitate the interpretation compared to frame images (Figure 1).

2.4 Earlier studies in forest reflectance anisotropy and image-based tree species recognition

Photogrammetric tree species recognition dates back 70 years (See references in Korpela, 2004). Work has mainly been based on the spectral properties (e.g. Rohde and Olson, 1972; Meyer et al., 1996; Haara and Haarala, 2002), but also on structural features in very-high resolution near-nadir data (Brandtberg, 1999, 2002; Eriksson, 2004). Using visual interpretation of large-scale colour-infrared (CIR) images, a classification accuracy of 95% was achieved in Finland (Korpela, 2007). These results give a baseline for the development of automatic methods.

Digitized CIR images were studied in monoscopic (Haara and Haarala, 2002) and multiview geometry (Korpela, 2004), and a higher, but too optimistically validated 78–90% classification accuracy was achieved, using multiview features representing Sun-lit and shaded parts of crowns.

In Sweden, Holmgren et al. (2008) used the PAN-sharpened CIR images of the DMC camera (Intergraph, Huntsville, USA). The multispectral (MS) images had a GSD of 60 cm. Using means of the three bands and 1711 trees, accuracies of 91% and 84% were achieved using October and June images, respectively. Tree crown delineation was done in dense LiDAR data.

In Finland, the UltraCam D (Vexcel Corporation, Boulder, CO, USA) images with discrete return LiDAR were tested for the classification of seedling stand vegetation in 5–12-yr-old plantations (Korpela et al., 2008) and in area-based estimation of the growing stock by species (Packalén et al., 2009). In seedling stands, image features were largely surpassed by LiDAR features in predicting power, while

in the estimation of the growing stock; band ratios RED/NIR and GRN/RED produced high model accuracy in the separation of LiDAR canopy hits from pine, spruce, and broadleaved trees.

At canopy level reflectance anisotropy has been studied in satellite image data (i.e. Rautiainen et al., 2008). The image scale has important implications. While in aerial imagery, a single crown can consist of hundreds of pixels, in commonly used satellite images multiple trees are represented by just one pixel. Newer high resolution satellites might achieve the same ground sample distance (GSD) as acquired by airborne remote sensing. The higher altitude of satellites might not be as relevant as one would assume first, because the majority of the atmospheric effects occur below 3–6 km.

At the level of sub-meter pixels, the content represents a mixture of branches and shoots. As a tree crown has no real surface, light rays also start to scatter inside the crown and on the same time this leads to branches dropping shadows on each other. These effects are usually examined when modelling the reflectance anisotropy by use of a physical model (i.e. Rautiainen, et al., 2004; Rautiainen and Stenberg, 2005).

3 Material and Methods

3.1 Study area and reference trees

The experiments were carried out in boreal forests of Hyytiälä, southern Finland (61°50'40"N, 24°17'13"E)¹. The trees reach maturity at ages between 80 and 130 years, when the dominant tree height is 21–33m on productive soils. The 15'197 reference trees used represent 121 plots with a size of 0.04–1.8 ha. Pine and spruce predominate the area and form mixed as well as pure stands. The birch stands are younger than 40 years. Isolated birches are found in coniferous stands (Korpela et al., 2010).

The plots are 130–198 m above sea level and the study area extends 2 x 6 km. The mires, which are frequent in the area, are largely drained and the (dominating) state-owned forests are mainly managed for commercial forestry.

For each tree in a plot, the position was measured (in the field with tacheometry, or by using aerial images and/or LiDAR, (Korpela et al. 2007, 2010) and additional forestry attributes like species, diameter-at-breast-height (DBH) and crown status (living normal, asymmetric, dying, oblique) were recorded. The material was restricted to LiDAR/Camera visible trees by doing a visual interpretation first. Most trees had a relative height of above 0.5. Thus the study applies to dominant, co-dominant and intermediate trees (Table 2, Table 3).

Site/age	Fertile-2	3	4	5	Barren-6	Sum
<40 yr.	586	2143	828	5	-	3562
40–60	79	4308	1614	-	2	6003
60–80	225	1544	138	43	25	1975
80–100	-	877	241	453	39	1610
100–120	72	1174	213	91	8	1558
>120 yr.	63	385	41	-	-	489
Sum	1025	10431	3075	592	74	15197

Table 2: Number of living pines, spruces, and birches in the different site fertilities (2–6) and age classes (yr.)

Variable	Pine N = 5914	Spruce N = 7105	Birch N = 2169
$d_{1.3}$, cm	20.1 (6.5)	20.3 (7.9)	15.1 (6.7)
h , m	17.5 (4.1)	18.1 (5.8)	16.4 (5.3)
d_{cr} , m	2.8 (0.9)	2.9 (0.9)	2.6 (0.9)
Age, yr.	59.5 (25.3)	66.4 (28.7)	47.0 (24.6)

Table 3: Mean and standard deviation (sdev) of tree variables in living pine, spruce, and birch trees

But as the delineation of tree crowns in images is a field of research by itself, and even though results from many of these methods might be rather good, we relied on the available, probably more accurate measurements from earlier research projects using the same area.

¹ WGS-84

3.2 ADS40-SH52 image data

The ADS40 flight was carried out on August 23, 2008 at 10–12 local (DST) time (GMT +3h) in 15 strips. Strips were named by using the starting time in GMT in the format “hhmm”. Solar elevation was 27.1°–37° and thus SZ was between 53° and 62.9°. The camera was installed with a stabilized mount in a Cessna Caravan aircraft and operated by an experienced pilot and camera operator. The multispectral images were registered in uncompressed mode. The PAN lines with a lossy compression were used only for aerial triangulation.

Multiple sensor lines were combined to configurations. Each sensor line records a certain amount of data, depending on the chosen compression. The integration time, which is set according to the targeted flying altitude and speed, defines the frequency, at which the data has to be transferred to the mass memory unit. As this transfer is limited by the transfer rate of the camera, the quantity and combination of sensor lines has to be chosen accordingly.

Table 4 shows the 12 sensor lines with their spectral band widths of the sensor (S/N 30120) used for the Hyytiälä experiment:

Name	Band position (FWHM), viewing direction	Used in configurations
REDN00A	604 – 656 nm, nadir	N00A
GRNN00A	532 – 581 nm, nadir	N00A
BLUN00A	440 – 492 nm, nadir	N00A
NIRN00A	830 – 896 nm, nadir	N00A
REDB16A	604 – 656 nm, backward 16°	B16A
GRNB16A	530 – 582 nm, backward 16°	B16A
BLUB16A	439 – 492 nm, backward 16°	B16A
NIRB16A	829 – 904 nm, backward 16°	B16A
PANF02A	500 – 659 nm, forward 2°	3 and 4 km strips
PANF02B	500 – 659 nm, forward 2°	NOT USED
PANB14A	498 – 658 nm, backward 14°	All strips
PANF27A	496 – 659 nm, forward 27°	All strips

Table 4: Available sensor lines and their spectral bandwidths

The nadir and backward multispectral data was recorded simultaneously at the 3 and 4 km altitudes. The 2-km nadir and backward data had to be collected separately, due to the low integration time needed at this altitude and the used CU40 data logger. Therefore flight lines of strips 0745 and 0753 were flown twice, changing the CCD configuration. The 1-km data acquired was not used here. (Table 5)

We used discrete-return LiDAR for crown modelling and for the determination of occlusions and shading (Section 3.3.4) and the data set consisted of three acquisitions in 2006–2008, which had a combined pulse density of 10–18 per m². The geometric match was verified to be better than 0.25 m in XY and Z (using natural and man-made targets). We also used a LiDAR-based terrain model with an RMS accuracy of 0.1–0.3 m.

Flying altitude	Start time [GMT]	Flight line azimuth	Sun Azimuth [°]	Sun Zenith [°]	Integration time [ms]	Active CCD lines (configuration)
2 km	0745	349	132.0	58.2	2.77	N00A
	0753	169	134.2	57.5	2.77	N00A
	0800	349	136.1	56.9	2.77	B16A
	0808	169	138.3	56.3	2.77	B16A
3 km	0818	349	141.1	55.6	4.16	N00A/B16A
	0825	169	143.1	55	4.16	N00A/B16A
	0833	260	145.4	54.5	4.16	N00A/B16A
4 km	0843	169	148.3	53.9	5.54	N00A/B16A
	0852	260	151.0	53.3	5.54	N00A/B16A

Table 5: ADS40-SH52 flight description. The GSD ranged from 10 cm at 1 km to 40 cm at 4 km altitude

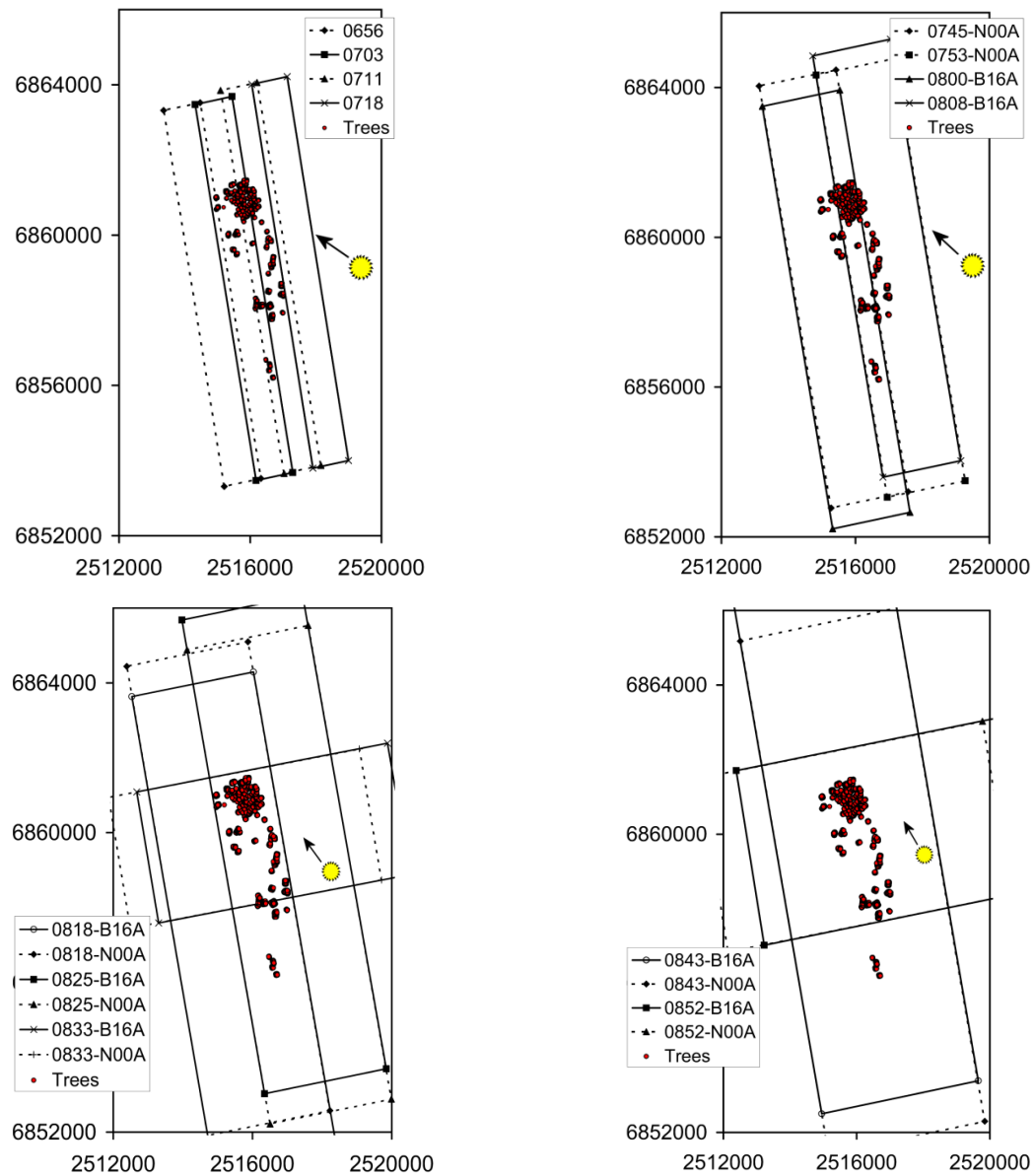


Figure 4: Geometry of the 1–4 km strips (from top left to bottom right). The coordinate system of the trees was in the national (Gauss-Kruger) Kartastokoordinaatijärjestelmä (now obsolete) with orthometric N60-heights. (Korpela et al., 2010)

3.3 Image processing and acquisition of image features for the reference trees

3.3.1 Image Postprocessing (ORIMA and XPro work)

Direct georeferencing (e.g. Cramer et al., 2000) was used in aerial triangulation with 59 signalized control points, which had been positioned using Network RTK. The direct georeferencing was based on the use of GPS/IMU and VRS-GPS (1 Hz) observations. Twelve points per strip were used for the adjustment using Leica ORIMA, while the remaining were validation points. Sub-pixel accuracy was reached for each of the image blocks from a certain altitude. The exterior orientation (EO) in six parameters was solved for each image line. The AT was done at the Finnish Geodetic Institute (FGI).

XPro produced so-called L1 epipolar images, rectified from the L0 (raw) data using the EO information from AT. The sensors recorded with 1Hz and a virtual reference station was set up. During this L1 rectification process, the atmospheric correction was applied using the default software settings. Also, the ASR data produced by XPro was in the L1-format.

Instead of storing each flight line in one image, XPro split the image into tiles (subimages) with a maximum size of 0.6 GByte. To avoid an even more tedious bookkeeping of subimages and their metafiles, the images were combined into simple, single-band (RAW) BIP-files with a maximal possible file size of 2 Gbyte, which was sufficient for the 2–4-km strips. These images could then be read by the KUVAMITT-program (Visual Basic / C, Win32 DPW), which was used for further processing of images, LiDAR and objects.

A combination of the atmospheric correction applied (ASR, ATM), flying time in GMT (hhmm), viewing angle (N00A, B16A), and spectral band (RED, GRN, BLU, NIR) was used as naming convention (i.e. ATM_0800_N00A_BLU.img).

In order to enable the use of all the different operations in KUVAMITT, a pushbroom sensor model for the ADS40 had been implemented, following example code provided by Leica Geosystems. Besides several modules, which were required by KUVAMITT to read and process the ADS40 image data, I also programmed an additional application to extract the angles needed in this thesis, using the exact position of the plane for every single crown point.

3.3.2 Visibility check for the reference trees

All the image strips were visually checked for any occlusions caused by clouds or shadows resulting from the cloud coverage during the campaign. Adding some extra buffer around these critical areas, they were digitized into (in the object space) polygons to be masked from the data.

For every image (RGBN x N00A-view or B16A-view), all tree top positions were tested for inclusion in the image (XYZ-to-L1 routine) and areas covered by clouds and shadows. Even though the in-situ horizontal visibility measurements indicated very good visibility (42–50 km) (Markelin et al., 2010), a few clouds at 700m altitude lead to loss of trees, which was different in each strip (Table 6). The loss reached 35.1% for the 3-km flight line 0833.

Flying altitude	Start time [GMT]	Active CCD configuration	Trees in image footprint	Trees occluded by cloud	Trees in cloud shadow	Trees lost [%]
1 km	0656	N00A	55	0	0	0
	0703	N00A	6987	531	0	7.6
	0711	N00A	11955	2802	85	24.1
	0718	N00A	0	0	0	0
	0725	N00A	6997	0	0	0
	0733	B16A	7037	0	0	0
2 km	0745	N00A	9599	308	0	3.2
	0753	N00A	13786	76	1019	7.9
	0800	B16A	9466	277	1306	16.7
	0808	B16A	13728	310	437	5.4
3 km	0818	N00A	15626	146	117	1.7
	0818	B16A	15626	0	48	0.3
	0825	N00A	15626	1683	772	15.7
	0825	B16A	15626	895	366	8.1
	0833	N00A	13743	1983	1843	27.8
	0833	B16A	13743	3933	912	35.1
4 km	0843	N00A	15626	204	392	3.8
	0843	B16A	15626	34	0	0.2
	0852	N00A	15110	283	601	5.9
	0852	B16A	15110	1533	166	11.2

Table 6: Tree occlusion by either clouds or their shadows

3.3.3 Crown modelling

If the geometry of the forest canopy is known, and multiple views are available so that the crown of a tree is visible from all sides, it is possible to sample the crown for the sun-lit and shaded spectra (Korpela, 2004; Larsen, 2007; Puttonen et al., 2009). For this purpose a crown envelope surface was modelled for each tree, using all the LiDAR points contained in a cylinder around the position of the stem. The selection was based on the diameter of the crown and a density factor df , which had values between 0.8 and 0.9 for dense stands and 1.1–1.2 for sparse and old stands.

Following the assumption of earlier researches (cf. Korpela, 2007), that the crown is represented by the upper 40% of the total tree height, and assuming that the form of a tree is rotational symmetric, following formula was used:

$$r = a^2 + b * h * \left(\frac{5}{2} * x_{rel} \right)^c \quad [5]$$

Using [5], crown forms typical to pine, spruce and birch can be modelled by adapting the three parameters a^2 , b , and c .

- a^2 Describes the flatness of the crown top. Using the squared value of a prevents the additive constant from becoming negative
- b Scale (where r is maximum at the base of the crown, $x_{rel} = 0.4$)
- c Defines the shape of the crown envelope, and it is convex if $c \leq 1$
- h Height of tree
- x_{rel} Relative offset from the top [0...0.4]

For each LiDAR point used, the corresponding values for r (distance to trunk) and x_{rel} (relative height to tree top) were determined (Figure 5) and stored to be used in observation equations.

The parameters were solved using weighted least-squares regression, where initial approximations of a^2 , b , and c were adjusted to final solution using the Gauss-Newton method (Jacobian used for linearization of [5]). Additional two observation equations and weights were used for parameters a^2 and c in order to keep them within plausible values (a^2 small and $c < 1$). Weights were applied to all observations of r , a^2 and c because of their different scales. The iteration used for the calculation (example iteration in Figure 6) stopped after 20 cycles or as soon as the absolute changes in parameters a , b , and c were smaller than 0.001.

For all 15627 trees, the mean RMSE was 0.35 m and the regression failed only for 60 trees. The values of c were between 0 and 0.91, which means that all crown envelopes were convex. This was necessary for testing the self-occlusion and self-shading attributes (Section 3.3.4)

An example of the resulting crown envelope is shown in Figure 7, superimposed in KUVAMITT using an UltraCam D, 1-km CIR image.

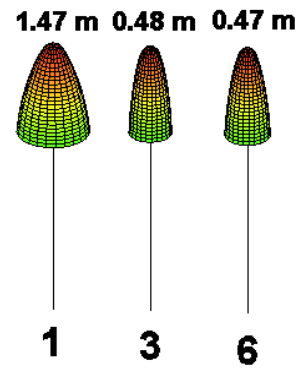
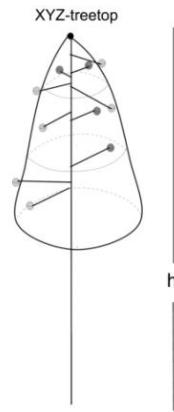


Figure 5: Transforming LiDAR points into observation pairs using the distance down from the top (x_{rel}) and the radius (XY-distance from the trunk) (Source: I. Korpela)

Figure 6: Iterations for the crown modelling algorithm and their corresponding RMSE (1: start of iteration with initial approximation of a^2, b and c ; 3: after three adjustments; 6: final solution) (Source: I. Korpela)



Figure 7: 40-year-old birch as seen in a stereo pair (UltraCam D, 1 km). The fitted crown is superimposed in the images. The XY-offsets in treetop positions and asymmetry of crowns (non circular) (in addition to image orientation errors) caused undoubtedly some errors when crowns were projected to the different images. (Source: I. Korpela)

3.3.4 Crown sampling

This 3D representation of the tree crown was then sampled in 121 different positions. In addition to the tree top, ten ‘rings’ were created at relative heights below the top, starting at 2.5% and moving down every 4% from the top to the base (38.5%, $x = 0.385$ in [5]) of the crown. While sampling the image, it became obvious, that even though we used aerial imagery, the scale of observation has important implications. While on the lowest level, a single crown is represented by hundreds of pixels, already at the altitude of 4 km different crown points ended up to be mapped to the same pixel. This has to be considered later on, when interpreting the pixel values of these crown points.

All 121 crown points were assigned to an illumination class, depending on whether they were occluded (or shaded) by the tree itself or another neighbouring tree. For this purpose of shadowing testing, all the LiDAR points were modelled as spheres with a diameter of 0.7 m and then tested for being in the line between tree and Sun, resp. tree and camera (Figure 8) for occlusion testing.

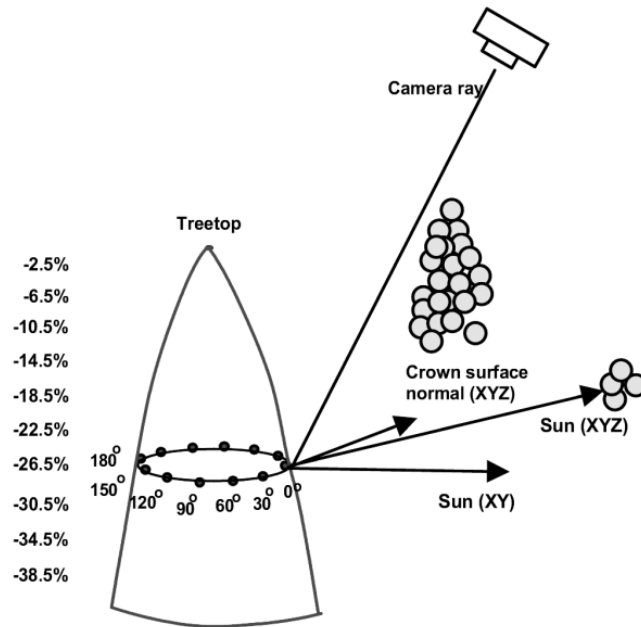


Figure 8: Heights of crown sampling and principle of using the LiDAR data (Korpela et al., 2010). The points were aligned towards the Sun and had a 30-degree azimuth difference. This resulted in 12 points per ring.

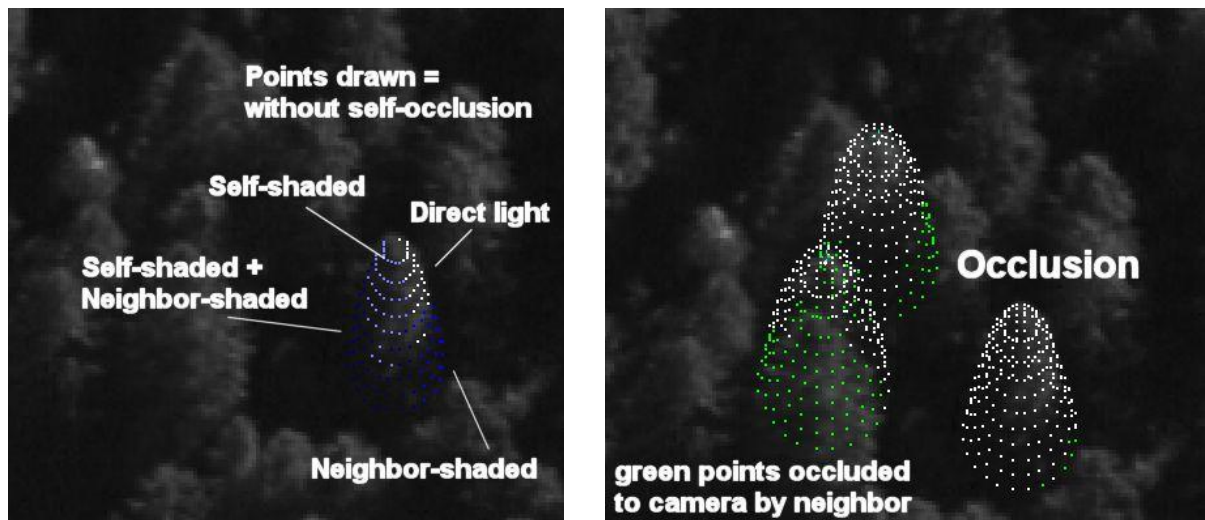


Figure 9: Images illustrating the accuracy of the ray tracing algorithm performed for each crown point (left: determination of different illumination classes, right: occlusion testing using neighbouring trees). ADS40 2-km data GRN band. (I. Korpela)

An overview of the different possible illumination classes is shown in Table 7:

	Self-occluded	Neighbour-occluded	Abbreviation
Sunlit	False	False	SL
Self-shaded	True	False	SS
Other-shaded	False	True	OS
Both-shaded	True	True	BS

Table 7: Possible illumination classes

When each of the 121 crown points was sampled for image data and determined for illumination class, also other geometric and angular data was collected for each crown point. These are given in Table 8.

Strip	hhmm atmospheric correction (ASR, ATM) view direction (N00A, B16A)
Tree information	Tree id Tree species Tree status Tree top height
Crown point features	Point id [1–121] Illumination class [SL,SS,OS,BS] Ring number [0–10] Offset to SA $pAngle$ [$0^\circ, \pm 30^\circ, \pm 60^\circ, \dots, \pm 150^\circ, 180^\circ$] Distance to camera d [m] Relative height (at 5-m, 10-m, 20-m radius) $h_{Rel1}, h_{Rel2}, h_{Rel3}$
Angular features	View Azimuth VA View Zenith VZ Signed View Zenith SVZ Sun Azimuth SA Sun Zenith SZ
Surface normal	3D vector XYZ
Band	RED, GRN, BLU, NIR, NDVI

Table 8: Available features (data) for each crown point in a tree

3.4 View illumination geometry

BRDF is defined by four angles: view zenith (VZ), view azimuth (VA), sun zenith (SZ) and sun azimuth (SA). According to Li and Strahler (1986), anisotropic effects are mainly caused by changes in the view geometry. As the acquisition time for a single strip is just a few minutes, it is assumed that the minor changes of the sun position can be neglected. Therefore SZ and SA don't change during the acquisition period. Because of the camera's design, VA in a nadir looking image is constant for all the trees on the same side of the aircraft. The only changing angle is VZ, which increases together with the planar distance (x) between tree and plane. Using basic geometry, VZ can be expressed using following equation (assuming vertical photography):

$$VZ = \text{atan}\left(\frac{x}{\Delta h}\right) \quad [6]$$

The equation shows, that VZ is also dependent on the height difference (Δh) between the crown point and the camera. Obviously, the flying altitude affects h and therefore it should be accounted for when comparing images with different image scale.

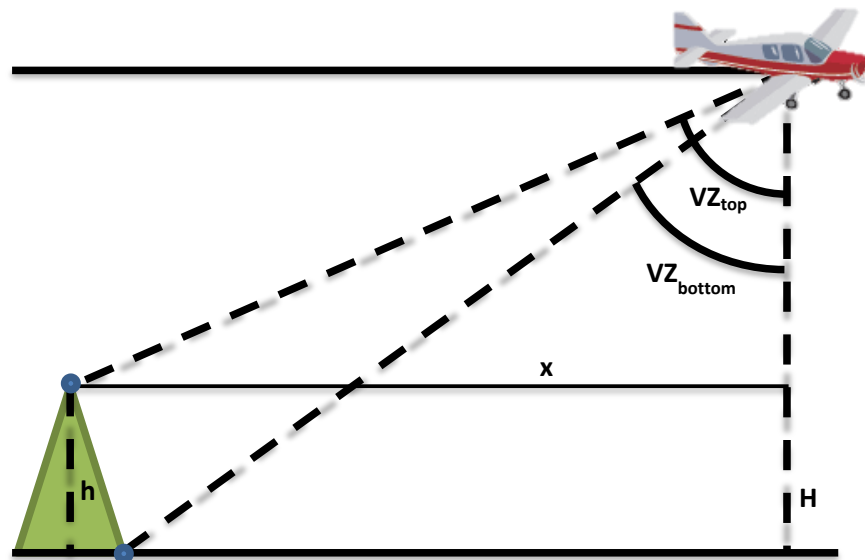


Figure 10: Changes in the VZ angle, for a point on the bottom of the crown compared to the top

Limiting the deviations to the effects caused by the different position on the plane created by one single line the equation becomes as following:

$$\Delta VZ = VZ_{top} - VZ_{bottom} \tag{7}$$

$$\Delta VZ = \text{atan}\left(\frac{x}{H-h}\right) - \text{atan}\left(\frac{x-w}{H}\right) \tag{8}$$

A quick calculation for the different flying altitudes and a tree with the average values for crown width and tree height shows that the differences for VZ are within a degree.

Flying altitude	ΔVZ [°] (centre)	ΔVZ [°] (border)
1 km	0.171	0.359
2 km	0.086	0.179
3 km	0.057	0.119
4 km	0.043	0.089

Table 9: Theoretical differences in VZ from the top to the bottom of the crown, using a crown width 3m width and 9m crown height

Due to the camera design, every line of the image has a different camera position, for which the projection centre data is stored (in so-called odf-files in ADS40). As the crown points are also located on different image lines, they have different camera positions as well (Figure 11).

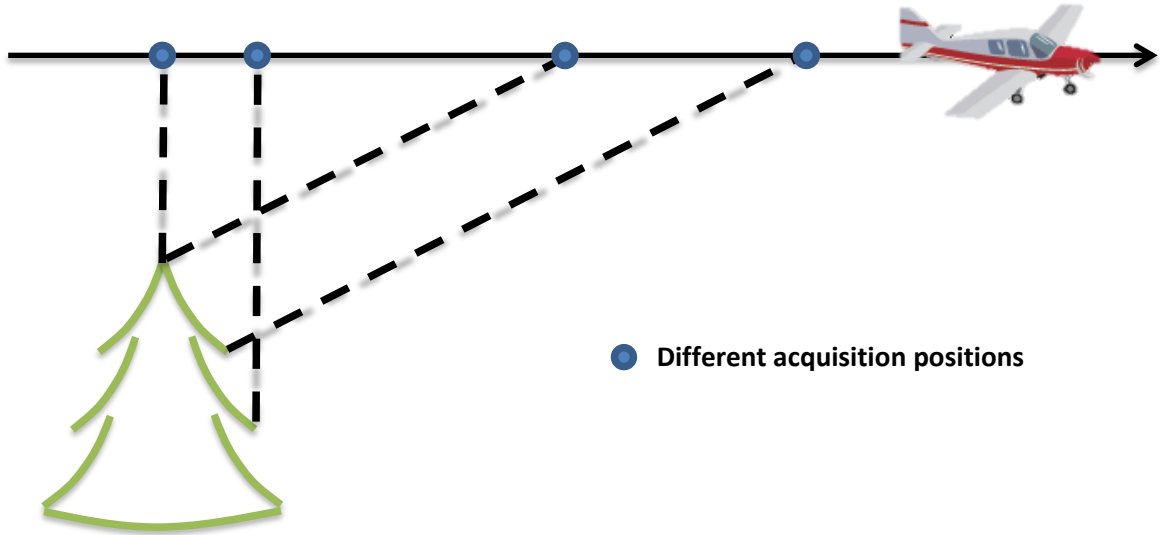


Figure 11: The image shows where different points are recorded for a N00A case (left) and also for the B16A case (right)

These differences in the camera position also contribute to the changes in VZ. To determine the precise angles of the viewing geometry, the exact position of the camera has to be extracted out of the ADS40 orientation files before calculating the corresponding angles. Table 10 gives an overview of all the different angles and their distribution:

Flight line	Side of plane	VA	VZ	SVZ
0745 N00A	Left	78.75 (0.76)	0.75 (0.24)	-0.75 (0.24)
	Right	259.3 (0.70)	19.36 (8.44)	19.36 (8.44)
0753 N00A	Right	79.45 (0.50)	14.02 (8.66)	14.02 (8.66)
0800 B16A	Right	299.31 (14.22)	25.70 (5.37)	-25.70 (5.37)
0808 B16A	Right	128.24 (16.87)	22.54 (5.35)	-22.54 (5.35)
0818 N00A	Right	259.35 (0.26)	18.24 (7.24)	18.24 (7.24)
0818 B16A	Right	300.66 (12.33)	24.61 (4.60)	24.61 (4.60)
0825 N00A	Right	79.37 (0.20)	13.33 (6.76)	13.33 (6.76)
0825 B16A	Right	129.95 (13.71)	21.30 (4.31)	21.30 (4.31)
0833 N00A	Left	349.71 (0.38)	14.27 (10.25)	-14.27 (10.25)
	Right	169.87 (0.26)	16.04 (9.57)	16.04 (9.57)
0833 B16A	Left	296.66 (21.70)	22.48 (6.64)	-22.48 (6.64)
	Right	216.18 (17.43)	23.58 (5.42)	23.58 (5.42)
0843 N00A	Left	259.33 (5.84)	4.89 (3.09)	-4.89 (3.09)
	Right	78.51 (6.64)	3.73 (3.02)	3.73 (3.02)
0843 B16A	Left	187.06 (10.07)	16.69 (0.95)	-16.19 (0.95)
	Right	156.83 (10.46)	16.30 (0.98)	16.30 (0.98)
0852 N00A	Left	349.49 (0.37)	14.19 (9.45)	-14.19 (9.45)
	Right	170.00 (0.74)	12.38 (6.46)	12.38 (6.46)
0852 B16A	Left	296.84 (20.36)	22.04 (5.89)	-22.04 (5.89)
	Right	220.62 (15.17)	21.25 (3.39)	21.25 (3.39)

Table 10: Flight lines with the means (and standard deviations) of the various angles calculated. Grey marked flight lines are using the B16A view.

3.5 Analysis of the success of the ATM correction using trees as reflectance targets

The first analysis was (the results are in section 4.1) about the differences in the anisotropy between the ASR and ATM data in a single flight line, separately for each illumination class, tree species, and spectral band. As a compromise between details in the image data and cost efficiency, the 30cm seems to be the most useful for commercial applications. Therefore first examinations were done using these images.

Due to the camera design, there are only two values for VA in one strip. One for trees situated on the left side of the tree and the other for the right side. Additionally, the flight path for the 2 – 4 km data was chosen to be on one side of the plane instead of flying over the area, thus reducing the data to just one VA angle per flight line (Figure 4).

Assuming that the atmospheric influence is proportional to the distance from the camera to the target (as showed in equation [6]), a linear effect dependent on the VZ is expected. The bigger the impact of the medium, the steeper will the slope of this linear dependency show up and also R^2 values should be high. Vice versa, if the applied atmospheric correction is working, the incline will be reduced for the ATM versions.

Ideally, the ATM data would show only the true anisotropy and its effect in VZ. This would imply that a change in flying altitude would also produce the comparable reflectance images, if the solar illumination geometry (SA/SZ) and the VA angle would remain the same.

To test if this hypothesis is true, for each flight line, the corresponding image pairs (ASR/ATM) were selected. Simple linear regression lines of the spectral response on the VZ angle were computed for every image. For comparison purposes between the at-sensor radiance (ASR) and the reflectance (ATM), all values needed to be normalised. To eliminate the influence of outliers, the mean of the subset was chosen as reference value instead of the maximum.

3.6 Effect of changes in the view-direction

Deering et al. (1994) mention, that the effects are more prominent when changing the view angle compared to differences in the solar zenith angle. To examine these effects and reduce the influence of other factors, the data was limited to the crown points situated in well sun-lit positions. Therefore only samples located in the direction of the Sun ($\rho\text{Angle}=0$) and with a relative height (h_{RelZ}) above 0.8 were selected. Using this subset of data, it was investigated, how much the values change when viewed from different directions. (Results are in section 4.2)

Depending on the flying direction, one should be aware of the illumination case being either front-lit or back-lit (Figure 1). In the case of a back-lit scene, the sunlit crown points are usually situated at the border of the visible area, also named “corona” further on. Observations in this area are to be handled carefully, because they seem to be mostly transparent (Li and Strahler, 1986). For this reason, the effects for points in the class of sun-lit pixels, were analysed using the N→S oriented 2-km strip 0808 and the 3-km strip 0825 (B16A views), which show strongly front-lit trees, while the S→N 2km 0800 and 3-km 0818 strip (B16A) were used for points in the self-shaded class.

To compare the fit (ATM data and VZ) of the linear to the non-linear regression, the residual standard error was calculated and compared.

3.7 Trends in vertical and horizontal direction

After carrying out the last two experiments, either all crown points for an illumination class (3.5) or only a small part on the top of the crown (3.6) was analysed. Results of this experiment can be found in section 5. In the following analysis I continued to take a closer look at each sampled position on the crown. The aim is to see, how light gets reflected on the crown surface, furthermore if there are better ways of sampling the crowns and weighting the observations to compensate for the anisotropy.

In order to compare the behaviour between tree species, the mean value of the spectral values at the top of the trees is calculated for all three species groups. Defining the top values as a reference for normalisation, also allows comparing the sun-lit and the self-shaded side of the trees.

The B16A data is used to obtain observations from both, the sun-lit and the backside of the trees.

For each position on the crown, the mean of the observed values are calculated and then divided by the reference value of the corresponding species. As a further indicator for the amount of anisotropy that is present for each species, the standard deviation (σ) of the calculated relative values will be determined. A low standard deviation will reveal that the relative reflectances are homogeneous for the whole crown, indicating that there is less anisotropy in this respective band. Because sun-lit and self-shaded points are expected to behave differently, σ will be calculated separately for each side of the tree.

3.8 Statistical methods

For the statistical analysis I used R (2.10.1, The R Foundation for Statistical Computing), SAS (9.2, SAS Institute Inc.), and Microsoft Excel (Office 2010, Microsoft Corp.). KUVAMITT programming was done in VB6.0 and C (Microsoft Visual Studio 6.0, Microsoft Corp.).

The non-linear weighted LS regression was implemented in KUVAMITT such that the normal equations were formed in KUVAMITT and the correction vector was solved using (Gauss-Newton) MATLAB routines in a DLL-function.

R was used for analysis of variance to compare distributions (aov), linear least square regression (lm), non-linear least square regression (nls) and for creating all plots (plot) and visual representations of the data.

The R^2 -value was calculated as indicator for the fit of a model. The least square regression already provided this information, for the non-linear-model, it was calculated using equation [9], where SS_{err} was determined by using the square of the Residual Standard Error (RSE), which is given by the nls-algorithm.

$$R^2 = 1 - \frac{SS_{err}}{SS_{total}} \quad [9]$$

4 Results of experiments

4.1 Evaluation of ATM correction with trees

The data was interpolated using a least square linear regression. As model, the simple assumption that only the SVZ explains the changes in the spectral reflectances was used. The R^2 -value was calculated for all regressions as an indicator for the quality of the fit.

In general, the ATM data showed a reduction for the slopes, which could be interpreted as an effect of the atmospheric correction. Bands in the visible spectra showed to be more influenced by SVZ than the NIR. This seems valid, as this data is known to be less affected by changes in the view geometry.

After introducing the ratio of the slope coefficients ATM/ASR, the effects of the atmospheric correction become visible. N→S strips (0753, 0825), where trees were seen back-lit, slopes show a ratio > 1, indicating that slopes in ATM are stronger than in ASR. In the opposite flying direction (0745, 0818; trees seen front-lit), values are usually between 0 and 1. Table 12 and Table 13 present all the slope coefficients and their ratios for the analysed flight lines.

At an altitude of 4 km (0843, 0852), the effect of the atmospheric correction seems to be reduced, as the slope coefficients remain around 1. This could either be, because the effect of the atmospheric correction is less prominent, due to the slightly smaller variation in SVZ (Table 10), or because at this height, trees are situated closer to the flight path, which generally leads to smaller values for SVZ. Additionally, for this strip, trees were situated on both sides of the plane, so that the effect of the front-lit trees eliminates the influence of the back-lit trees. With a flight path from east to west, trees on the side of image 0852 are highly front- or back-lit. Additionally, trees are also spread across the whole range of SVZ. This leads to a high dependency on SVZ in ASR and ATM, which can be seen in the R^2 -values, which was in average (for all bands and species) 26.8% for SL points and 20.6% for SS points in the ATM version of the images.

A different behaviour between flight lines with changing flying direction was observed when examining the R^2 -values. While in the ASR data up to 23.1% of the variation in BLU (for SL points in Pine) could be explained by changes in SVZ for strips towards north, the maximum value in the southbound images was for Spruce and only 8.9%. On the other hand, after applying the atmospheric correction, variations in Spectra were better explained by SVZ for strips flying from north to south. The same effect can be observed for self-shaded points (Table 11)

SL	Max R^2 (ASR, N→S)	Max R^2 (ASR, S→N)	Max R^2 (ATM, N→S)	Max R^2 (ATM, S→N)
Pine	5.9% (BLU 0843)	23.1% (BLU 0753)	16.8% (BLU 0745)	7.2% (BLU 0753)
Spruce	8.9% (BLU 0745)	3.7% (BLU 0753)	32.3% (BLU 0745)	3.4% (BLU 0825)
Birch	3.7% (BLU 0745)	6.9% (BLU 0753)	14.9% (BLU 0745)	1.5% (BLU 0753)
SS				
Pine	4.2% (BLU 0843)	32.3% (BLU 0753)	10.0% (BLU 0818)	13.6% (BLU 0753)
Spruce	3.4% (BLU 0843)	20.4% (BLU 0753)	12.0% (BLU 0745)	6.6% (BLU 0753)
Birch	4.4% (NIR 0818)	17.5% (BLU 0753)	5.6% (NDVI 0818)	5.8% (BLU 0753)

Table 11: Maximum values of R^2 for sun-lit and self-shaded crown points

In general, the maximum values for R^2 were observed in the BLU band, only for SS points on birch trees in N→S strips, NIR (in ASR) resp. NDVI (in ATM) had higher values.

For the sun-lit points, out of the four different combinations (N→S/S→N, ASR/ATM) the one with the highest R^2 -value are shown (Figure 12, Figure 13). The images illustrate, that mainly the slope is responsible for the explanatory power of SVZ.

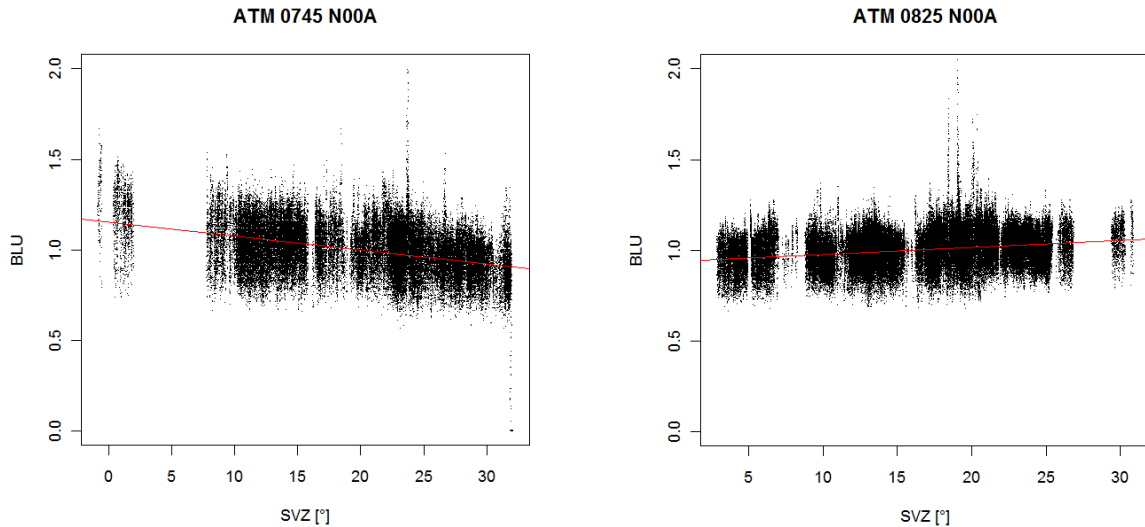


Figure 12: Images show ATM data of SL points of pines in the BLU band, explained by SVZ. The left plot shows a N→S strip (0745) and its linear regression with a R^2 -value of 32.27%. As comparison on the right, a S→N strip (0825), where the R^2 -value was much lower (3.41%).

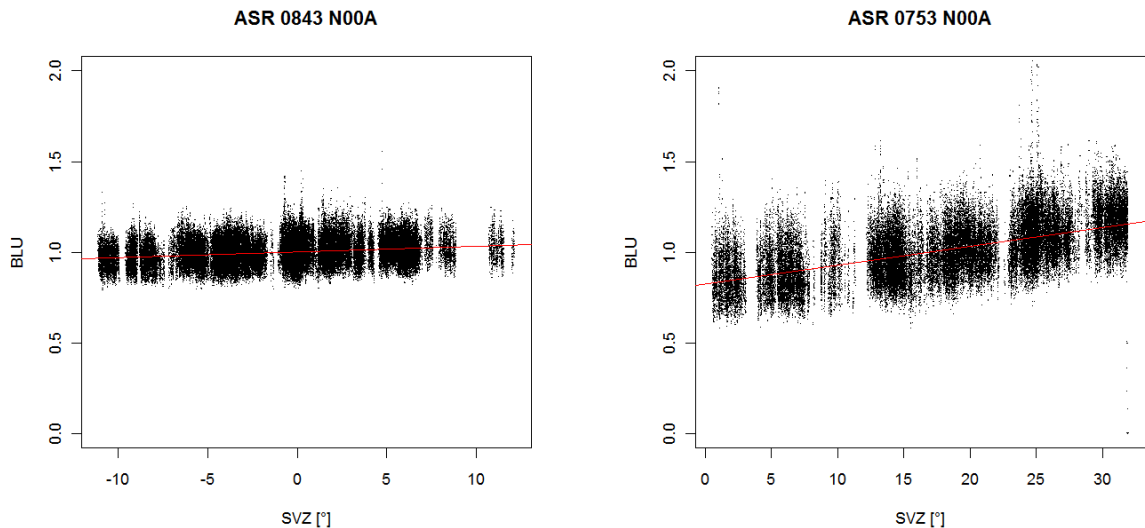


Figure 13: Images show ASR data of SS points of spruces in the BLU band, explained by SVZ. The left plot shows a N→S strip (0843) and its linear regression with a low R^2 -value of 4.19%. As comparison on the right, a S→N strip (0753), where the R^2 -value was much higher (32.31%).

As mentioned before, a reduced slope is assumed to be expected after applying the atmospheric correction. Therefore, the behaviour for the N→S lines matches to what was expected. As I used the N00A configuration for this analysis, tree tops are equally split between sun-lit and back-lit in the centre of the image, but the more trees are situated away from the centre line, the sun-lit side dominates. This leads to the assumption, that the atmospheric correction is mainly successful for sun-lit points. Heikkinen et al. (2010) point out, that for the algorithm used for the atmospheric correction, only sun-lit areas have the corresponding illumination properties. The odd behaviour of

SL points on the backside of the tree could be explained by these points being mostly situated in the area of the corona, where various errors can contribute to the observed effects.

	Pine			Spruce			Birch			
	ASR	ATM	ATM/ASR	ASR	ATM	ATM/ASR	ASR	ATM	ATM/ASR	
RED	0745	-0.0041	-0.0075	1.84	<u>-0.0105</u>	<u>-0.0140</u>	1.34	-0.0048	-0.0069	1.44
	0753	0.0067	0.0043	0.63	0.0046	0.0020	0.44	0.0031	0.0013	0.43
	0818	-0.0042	-0.0068	1.62	-0.0058	-0.0091	1.58	0.0000	-0.0022	-57.41
	0825	0.0060	0.0040	0.66	0.0020	-0.0002	-0.07	-0.0006	-0.0022	3.91
	0843	0.0049	0.0048	0.98	0.0049	0.0048	0.99	-0.0010	-0.0009	0.88
	*0852	<u>0.0091</u>	<u>0.0091</u>	1.00	<u>0.0115</u>	<u>0.0115</u>	1.00	<u>0.0076</u>	<u>0.0075</u>	0.98
GRN	0745	-0.0030	-0.0059	1.92	-0.0086	<u>-0.0114</u>	1.32	-0.0021	-0.0039	1.87
	0753	0.0053	0.0032	0.60	0.0036	0.0016	0.44	0.0038	0.0023	0.61
	0818	-0.0025	-0.0047	1.85	-0.0042	-0.0068	1.60	0.0012	-0.0006	-0.53
	0825	0.0044	0.0027	0.61	0.0008	-0.0009	-1.07	-0.0002	-0.0015	8.43
	0843	0.0035	0.0035	0.99	0.0034	0.0035	1.00	-0.0008	-0.0007	0.88
	*0852	<u>0.0086</u>	<u>0.0085</u>	1.00	<u>0.0108</u>	<u>0.0108</u>	1.00	<u>0.0079</u>	<u>0.0078</u>	0.99
BLU	0745	-0.0022	<u>-0.0078</u>	3.52	<u>-0.0050</u>	<u>-0.0103</u>	2.08	-0.0039	<u>-0.0080</u>	2.05
	0753	<u>0.0081</u>	<u>0.0040</u>	0.49	<u>0.0071</u>	0.0030	0.42	<u>0.0060</u>	0.0026	0.43
	0818	-0.0026	<u>-0.0065</u>	2.51	<u>-0.0029</u>	<u>-0.0074</u>	2.54	-0.0015	<u>-0.0052</u>	3.43
	0825	<u>0.0066</u>	<u>0.0038</u>	0.58	<u>0.0057</u>	0.0028	0.49	0.0037	0.0010	0.27
	0843	<u>0.0037</u>	<u>0.0051</u>	1.37	<u>0.0043</u>	<u>0.0061</u>	1.43	0.0017	0.0024	1.43
	*0852	<u>0.0096</u>	<u>0.0106</u>	1.10	<u>0.0111</u>	<u>0.0124</u>	1.12	<u>0.0097</u>	<u>0.0104</u>	1.07
NIR	0745	-0.0017	-0.0017	1.02	-0.0082	-0.0082	1.00	-0.0011	-0.0010	0.95
	0753	-0.0005	-0.0005	1.01	0.0011	0.0011	1.01	0.0024	0.0024	1.03
	0818	0.0017	0.0017	0.98	-0.0041	-0.0041	1.01	0.0048	0.0048	1.01
	0825	-0.0011	-0.0011	1.00	-0.0008	-0.0008	0.99	-0.0053	-0.0052	0.99
	0843	-0.0022	-0.0021	1.00	0.0021	0.0021	1.00	-0.0050	-0.0050	1.00
	*0852	<u>0.0059</u>	<u>0.0059</u>	1.00	<u>0.0094</u>	<u>0.0094</u>	1.00	<u>0.0083</u>	<u>0.0083</u>	1.00
NDVI	0745	0.0002	0.0009	5.65	0.0000	0.0009	19.00	0.0010	0.0012	1.21
	0753	<u>-0.0049</u>	-0.0022	0.46	-0.0017	-0.0002	0.12	-0.0005	0.0003	-0.69
	0818	0.0032	<u>0.0028</u>	0.89	0.0007	0.0014	2.04	0.0024	<u>0.0022</u>	0.92
	0825	<u>-0.0045</u>	-0.0019	0.43	-0.0015	-0.0001	0.10	-0.0025	-0.0010	0.40
	0843	-0.0044	-0.0026	0.59	-0.0016	-0.0010	0.61	-0.0025	-0.0016	0.64
	*0852	<u>-0.0023</u>	<u>-0.0013</u>	0.58	-0.0007	-0.0005	0.69	0.0006	0.0004	0.62

Table 12: Slope coefficients (and their ratio) for the least-squares regression lines using sun-lit points. N→S strips are marked grey, * indicates E→W strip 0852. Slopes, where the model had an R²-value of above 0.05 are underlined.

		Pine			Spruce			Birch		
		ASR	ATM	ATM/ASR	ASR	ATM	ATM/ASR	ASR	ATM	ATM/ASR
RED	0745	0.0009	-0.0034	-3.63	0.0033	-0.0021	-0.62	0.0055	0.0017	0.31
	0753	<u>0.0103</u>	0.0065	0.63	0.0089	0.0042	0.48	0.0061	0.0028	0.45
	0818	-0.0014	-0.0048	3.37	0.0021	-0.0026	-1.28	0.0072	0.0037	0.51
	0825	0.0100	0.0070	0.70	0.0044	0.0009	0.21	0.0045	0.0017	0.37
	0843	0.0031	0.0031	1.00	0.0003	0.0006	1.84	-0.0041	-0.0038	0.91
	*0852	<u>0.0046</u>	<u>0.0052</u>	1.14	<u>0.0052</u>	<u>0.0062</u>	1.20	0.0045	<u>0.0051</u>	1.12
GRN	0745	0.0007	-0.0031	-4.79	0.0038	-0.0007	-0.18	0.0060	0.0027	0.45
	0753	0.0084	0.0052	0.62	0.0072	0.0036	0.50	0.0054	0.0027	0.49
	0818	-0.0005	-0.0034	6.55	0.0025	-0.0013	-0.51	0.0071	0.0041	0.58
	0825	0.0075	0.0050	0.67	0.0024	-0.0002	-0.08	0.0033	0.0011	0.32
	0843	0.0028	0.0028	1.00	-0.0003	0.0000	0.12	-0.0035	-0.0032	0.91
	*0852	<u>0.0055</u>	<u>0.0060</u>	1.09	<u>0.0059</u>	<u>0.0067</u>	1.13	<u>0.0047</u>	<u>0.0051</u>	1.09
BLU	0745	0.0007	<u>-0.0057</u>	-7.98	0.0009	<u>-0.0056</u>	-6.00	0.0013	<u>-0.0041</u>	-3.11
	0753	<u>0.0104</u>	<u>0.0057</u>	0.55	<u>0.0097</u>	<u>0.0047</u>	0.49	<u>0.0089</u>	<u>0.0046</u>	0.51
	0818	-0.0009	<u>-0.0052</u>	5.84	0.0003	<u>-0.0046</u>	-13.43	0.0020	-0.0023	-1.13
	0825	<u>0.0084</u>	<u>0.0054</u>	0.64	<u>0.0070</u>	<u>0.0037</u>	0.54	<u>0.0067</u>	<u>0.0036</u>	0.54
	0843	0.0030	0.0043	1.43	0.0026	0.0040	1.54	0.0008	0.0014	1.76
	*0852	<u>0.0085</u>	<u>0.0104</u>	1.21	<u>0.0091</u>	<u>0.0117</u>	1.28	<u>0.0092</u>	<u>0.0110</u>	1.20
NIR	0745	0.0004	0.0002	0.55	0.0040	0.0038	0.95	0.0076	0.0075	0.99
	0753	0.0025	0.0024	0.95	0.0039	0.0038	0.96	0.0020	0.0019	0.98
	0818	0.0037	0.0036	0.96	0.0032	0.0030	0.94	0.0116	0.0116	0.99
	0825	0.0024	0.0023	0.96	-0.0002	-0.0003	1.68	-0.0047	-0.0047	1.00
	0843	-0.0024	-0.0024	0.99	-0.0032	-0.0032	0.99	-0.0109	-0.0108	1.00
	*0852	<u>0.0054</u>	<u>0.0054</u>	1.00	<u>0.0067</u>	<u>0.0068</u>	1.01	<u>0.0058</u>	<u>0.0058</u>	1.00
NDVI	0745	-0.0014	0.0005	-0.32	-0.0005	0.0015	-2.71	0.0002	0.0011	4.63
	0753	<u>-0.0049</u>	-0.0018	0.37	-0.0027	-0.0003	0.10	-0.0020	-0.0002	0.11
	0818	0.0028	0.0030	1.06	0.0005	0.0019	3.58	0.0023	<u>0.0025</u>	1.09
	0825	-0.0045	-0.0016	0.36	-0.0027	-0.0005	0.18	-0.0044	-0.0019	0.43
	0843	-0.0033	-0.0020	0.60	-0.0025	-0.0016	0.66	-0.0039	-0.0025	0.65
	*0852	0.0012	0.0004	0.34	0.0014	0.0004	0.26	0.0008	0.0003	0.32

Table 13: Slope coefficients (and their ratio) for the least-squares regression lines using self-shaded points. N→S strips are marked grey, * indicates E→W strip 0852. Slopes, where the model had an R²-value of above 0.05 are underlined.

4.2 Influence of view azimuth direction

To limit the observations to cases which are well defined, only the top of the tree is considered. Limiting to points where the relative height (h_{Rel2}) is above 0.8 also eliminated trees, which are most likely not affected by any higher neighbours. Unfortunately this also reduced the number of birch trees available, because birch tree in this area were planted later than the other species, and therefore are younger and smaller.

The non-linear model chosen was a simple quadratic function, as described in the following formula:

$$f(VA) = a * VA^2 + b * VA + c \quad [10]$$

Even though improvements were sometimes small, the non-linear regression showed to have a higher R^2 -value for all species and bands, not only for SL but also SS points.

For the sun-lit part of the crown, the mean of the differences between linear and non-linear model was 0.012 and the maximum was observed for the BLU values of pines in the 0808 strip (0.061) (Figure 14, left). SL points showed for most cases an almost linear trend. Accordingly, the improvements in the R^2 -values were smaller when using the non-linear model.

The sun-lit part of the part overall showed higher values for R^2 , and the average difference between SL and SS was 0.063. For self-shaded points, the maximal difference of R^2 reached 0.025 for pines as well, but in the 0818 flight line (Figure 14, right).

Sun-lit points sometimes showed an almost linear trend, which explains the lower values for the difference in R^2 . The maximum improvement was 1.35%, also for the BLU values of pines, but in the 0825 strip (Figure 14, left). BLU differed from the other bands, as it always showed higher improvements when using the non-linear model instead of the linear regression. Maybe this is the reason why self-shaded points in the BLU spectra showed to be a good predictor for tree species in Korpela et al. (2010).

To eliminate any strip-specific influences, the R^2 -value was averaged between observations in the 20 and 30 cm data. An overview of these values and their improvement when using the non-linear model is shown in Table 14.

		SL			SS		
		R ² linear	R ² non-linear	Δ	R ² linear	R ² non-linear	Δ
Pine	RED	0.004	0.027	0.023	0.005	0.006	0.001
	GRN	0.001	0.012	0.011	0.017	0.019	0.001
	BLU	0.210	0.265	0.055	0.021	0.035	0.014
	NIR	0.005	0.011	0.006	0.003	0.005	0.002
	NDVI	0.020	0.036	0.016	0.017	0.019	0.002
Spruce	RED	0.007	0.008	0.000	0.004	0.006	0.002
	GRN	0.025	0.025	0.000	0.004	0.007	0.002
	BLU	0.328	0.360	0.031	0.003	0.011	0.009
	NIR	0.022	0.022	0.000	0.005	0.012	0.007
	NDVI	0.027	0.028	0.000	0.001	0.012	0.011
Birch	RED	0.018	0.018	0.000	0.003	0.005	0.003
	GRN	0.048	0.049	0.001	0.008	0.012	0.003
	BLU	0.114	0.123	0.010	0.004	0.013	0.009
	NIR	0.061	0.075	0.014	0.007	0.007	0.000
	NDVI	0.047	0.061	0.014	0.002	0.005	0.004

Table 14: Coefficient of determination R² for the linear and non-linear least squares regression. Δ shows the difference between the R²-value of the linear and non-linear model.

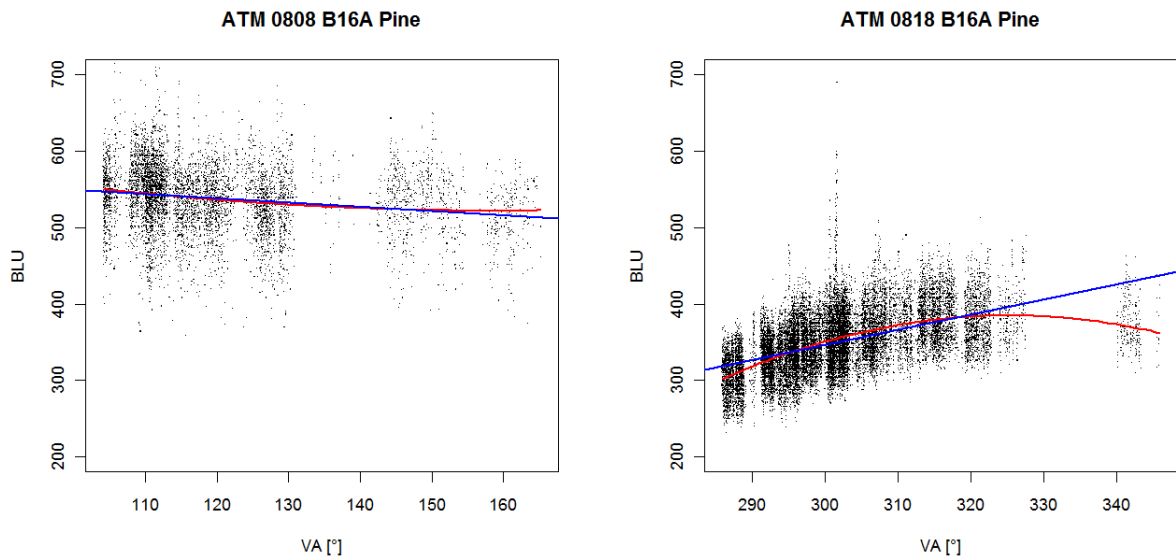


Figure 14: Examples with the largest improvement in R² when using a non-linear regression instead of the linear model for SL points of well front-lit trees (left, R²=0.061) and SS points of well back-lit trees (right, R²=0.026).

4.3 Intracrown variation

Analysing the tree crown revealed that in average, the relative reflectances on the SL side are 30% higher than on the SS part of the crown. Pines showed to have less anisotropy compared to spruce and birch in SL. Comparing the different bands, BLU had the lowest variation in the crown. Even in the near-infrared spectrum, all species showed to have more anisotropy. This could be caused by applying the atmospheric correction. Over all, values in the tree crown ranged from 0.794 to 1.531 in SL and from 0.428 to 1.128 (Table 15) in SS.

By arranging the values in a table and colouring each cell corresponding to its value, the resulting image visualises nicely the different behaviour of each species (Table 16, Table 17, and Table 18).

The first look at the data already confirms the assumption, that points located towards the sun and almost at the top are the brightest. For all species and bands, 8 out of the 12 maximum reflectance points on the sun-lit side were situated on the second layer from the top. In horizontal direction even 10/12 points were in the direction of the sun.

While for pine and spruce, the highest points on the back side of the tree are illuminated the same amount as the top, for birch the decrease of lightening already starts on the first layer. This could be related to the form of birch trees being flat at the top. As the relative height was not accounted for when creating the relative values, this effect could also originate from birch trees being younger and therefore smaller as their surrounding pine and spruce trees.

Another effect, which was not considered when creating this tree crown analysis, was the contribution of illumination by neighbouring trees as shown by Korpela et al. (2010). This might not affect the birch trees being darker on the shaded side of the crown as birch trees showed to have a stronger influence affecting pine and spruce than being illuminated by them. But brightness for pine and spruce trees showed to be influenced up to 23% by surrounding trees.

		SL			SS		
		Min	Max	σ	Min	Max	σ
Pine	RED	0.955	1.274	0.086	0.701	1.035	0.096
	GRN	0.927	1.226	0.080	0.618	1.006	0.111
	BLU	0.961	1.082	0.028	0.876	1.010	0.038
	NIR	0.816	1.278	0.123	0.428	1.023	0.165
Spruce	RED	0.967	1.482	0.136	0.676	1.075	0.094
	GRN	0.964	1.407	0.119	0.618	1.060	0.101
	BLU	0.998	1.136	0.037	0.906	1.020	0.029
	NIR	0.971	1.517	0.146	0.478	1.128	0.139
Birch	RED	0.937	1.464	0.135	0.554	0.948	0.091
	GRN	0.917	1.432	0.131	0.563	0.953	0.088
	BLU	0.927	1.134	0.051	0.810	0.981	0.044
	NIR	0.794	1.531	0.185	0.465	1.022	0.134

Table 15: Minimum, maximum and standard deviation for the relative reflectances separated for the sun-lit and self-shaded part of the crown

Pine

	-90	-60	-30	0	30	60	90	-120	-150	180	150	120
RED	0.955	1.048	1.155	1.240	1.242	1.137	0.983	1.029	1.035	1.024	1.022	1.002
	0.971	1.066	1.168	1.252	1.262	1.162	1.008	1.019	0.993	0.956	0.976	0.992
	0.989	1.076	1.171	1.249	1.259	1.170	1.028	1.003	0.950	0.897	0.927	0.975
	1.008	1.094	1.176	1.251	1.263	1.180	1.050	0.981	0.907	0.849	0.879	0.949
	1.018	1.105	1.177	1.256	1.272	1.172	1.062	0.956	0.876	0.814	0.835	0.926
	1.028	1.113	1.185	1.264	1.274	1.160	1.061	0.931	0.845	0.781	0.808	0.898
	1.047	1.114	1.174	1.258	1.256	1.148	1.059	0.909	0.823	0.760	0.774	0.873
	1.048	1.113	1.154	1.250	1.247	1.121	1.050	0.879	0.804	0.742	0.755	0.851
	1.028	1.090	1.127	1.228	1.233	1.075	1.037	0.858	0.783	0.720	0.740	0.811
	0.987	1.071	1.035	1.067	1.154	1.025	0.983	0.806	0.777	0.701	0.724	0.808
GRN	0.948	1.043	1.152	1.226	1.222	1.134	0.989	1.006	0.986	0.968	0.983	0.978
	0.959	1.061	1.158	1.220	1.223	1.149	1.013	0.978	0.917	0.878	0.919	0.953
	0.980	1.068	1.151	1.204	1.204	1.146	1.027	0.946	0.859	0.810	0.859	0.923
	0.997	1.077	1.145	1.193	1.191	1.138	1.038	0.908	0.808	0.757	0.805	0.887
	1.002	1.079	1.132	1.181	1.180	1.119	1.034	0.873	0.771	0.717	0.757	0.856
	1.005	1.076	1.126	1.165	1.156	1.094	1.027	0.840	0.735	0.683	0.725	0.821
	1.019	1.071	1.104	1.143	1.125	1.063	1.013	0.812	0.712	0.661	0.693	0.792
	1.007	1.057	1.072	1.115	1.094	1.030	0.991	0.777	0.691	0.644	0.675	0.768
	0.990	1.031	1.032	1.080	1.067	0.983	0.968	0.757	0.675	0.631	0.659	0.731
	0.947	1.006	0.955	0.945	0.987	0.935	0.927	0.716	0.674	0.618	0.645	0.719
BLU	0.992	1.022	1.053	1.076	1.074	1.043	1.000	1.007	1.010	1.007	1.005	1.001
	0.995	1.027	1.058	1.081	1.082	1.052	1.008	1.000	0.994	0.984	0.986	0.991
	0.994	1.028	1.055	1.076	1.078	1.052	1.013	0.991	0.978	0.962	0.967	0.980
	0.996	1.029	1.051	1.071	1.074	1.051	1.017	0.981	0.961	0.943	0.947	0.967
	0.995	1.026	1.044	1.068	1.071	1.045	1.016	0.971	0.948	0.928	0.931	0.958
	0.992	1.025	1.043	1.062	1.064	1.037	1.014	0.962	0.935	0.915	0.920	0.945
	0.995	1.023	1.033	1.055	1.053	1.030	1.008	0.954	0.927	0.906	0.904	0.935
	0.990	1.016	1.022	1.047	1.042	1.016	1.002	0.945	0.918	0.897	0.897	0.927
	0.980	1.007	1.011	1.032	1.033	0.997	0.996	0.938	0.905	0.888	0.892	0.911
	0.961	0.995	0.982	0.985	1.004	0.982	0.976	0.917	0.902	0.876	0.887	0.905
NIR	0.961	1.069	1.188	1.268	1.263	1.166	1.001	1.023	0.978	0.942	0.950	0.946
	0.985	1.088	1.205	1.278	1.276	1.189	1.030	0.968	0.867	0.819	0.862	0.901
	1.018	1.099	1.198	1.256	1.243	1.175	1.046	0.905	0.777	0.722	0.779	0.854
	1.040	1.101	1.183	1.226	1.207	1.147	1.049	0.838	0.698	0.642	0.703	0.803
	1.045	1.096	1.154	1.192	1.166	1.103	1.032	0.775	0.636	0.579	0.635	0.752
	1.047	1.086	1.127	1.143	1.114	1.053	1.011	0.718	0.581	0.526	0.585	0.702
	1.045	1.056	1.078	1.085	1.047	0.996	0.969	0.669	0.538	0.486	0.536	0.657
	1.037	1.022	1.017	1.029	0.988	0.942	0.936	0.618	0.507	0.461	0.504	0.616
	0.999	0.984	0.954	0.954	0.954	0.883	0.889	0.588	0.481	0.439	0.479	0.579
	0.946	0.935	0.869	0.816	0.841	0.828	0.835	0.546	0.486	0.428	0.459	0.547

Table 16: Relative reflectances for pine trees, calculated using the mean of the tree top as reference. Column depict offset to Sun and rows correspond to relative heights of 2.5%...38.5% down from treetop.

Spruce

	-90	-60	-30	0	30	60	90	-120	-150	180	150	120
RED	0.996	1.131	1.287	1.373	1.317	1.139	0.967	1.075	1.011	0.991	1.010	0.973
	1.032	1.178	1.349	1.448	1.375	1.173	0.982	1.051	0.925	0.891	0.968	0.974
	1.071	1.212	1.373	1.465	1.400	1.201	1.009	1.030	0.884	0.827	0.923	0.967
	1.103	1.237	1.385	1.482	1.417	1.216	1.041	1.008	0.855	0.787	0.884	0.957
	1.131	1.260	1.382	1.480	1.416	1.226	1.065	0.984	0.829	0.757	0.850	0.940
	1.146	1.270	1.383	1.462	1.392	1.224	1.076	0.965	0.812	0.737	0.822	0.923
	1.151	1.263	1.369	1.452	1.374	1.208	1.087	0.933	0.793	0.718	0.799	0.910
	1.148	1.246	1.346	1.405	1.362	1.199	1.081	0.915	0.774	0.705	0.782	0.891
	1.139	1.241	1.309	1.374	1.329	1.168	1.067	0.903	0.771	0.691	0.764	0.878
	1.121	1.195	1.218	1.233	1.247	1.138	1.071	0.890	0.780	0.676	0.749	0.851
GRN	0.979	1.116	1.273	1.363	1.310	1.140	0.964	1.060	0.983	0.962	0.979	0.934
	1.012	1.150	1.314	1.407	1.340	1.159	0.975	1.012	0.871	0.844	0.919	0.920
	1.047	1.175	1.323	1.395	1.335	1.167	0.994	0.976	0.820	0.771	0.871	0.906
	1.073	1.188	1.315	1.395	1.337	1.170	1.012	0.939	0.782	0.727	0.828	0.891
	1.094	1.202	1.304	1.375	1.321	1.169	1.030	0.913	0.753	0.697	0.794	0.874
	1.101	1.201	1.296	1.346	1.288	1.162	1.032	0.891	0.733	0.674	0.764	0.855
	1.099	1.194	1.270	1.326	1.266	1.140	1.042	0.863	0.718	0.657	0.739	0.842
	1.084	1.173	1.246	1.278	1.248	1.119	1.035	0.841	0.699	0.647	0.722	0.819
	1.081	1.169	1.220	1.251	1.220	1.095	1.012	0.826	0.697	0.629	0.701	0.809
	1.059	1.118	1.135	1.118	1.146	1.060	1.015	0.817	0.701	0.618	0.687	0.782
BLU	1.014	1.051	1.087	1.104	1.086	1.042	0.998	1.020	1.016	1.009	1.007	1.004
	1.023	1.064	1.105	1.127	1.106	1.053	1.003	1.016	1.000	0.987	0.991	0.996
	1.031	1.070	1.109	1.132	1.113	1.061	1.012	1.012	0.987	0.969	0.977	0.988
	1.036	1.073	1.110	1.136	1.118	1.065	1.019	1.004	0.976	0.953	0.966	0.980
	1.040	1.075	1.107	1.132	1.115	1.065	1.025	0.998	0.966	0.943	0.955	0.975
	1.040	1.075	1.105	1.126	1.106	1.060	1.023	0.992	0.957	0.933	0.946	0.968
	1.038	1.071	1.097	1.119	1.098	1.054	1.024	0.980	0.948	0.924	0.938	0.964
	1.035	1.062	1.089	1.105	1.092	1.044	1.019	0.977	0.941	0.917	0.932	0.959
	1.031	1.059	1.079	1.093	1.081	1.033	1.014	0.970	0.936	0.910	0.925	0.955
	1.023	1.043	1.046	1.054	1.052	1.023	1.015	0.965	0.938	0.906	0.919	0.942
NIR	1.003	1.171	1.364	1.474	1.419	1.210	0.971	1.128	1.041	0.983	0.957	0.906
	1.043	1.208	1.405	1.517	1.451	1.233	0.989	1.052	0.884	0.837	0.880	0.871
	1.081	1.227	1.400	1.483	1.420	1.238	1.021	0.978	0.787	0.738	0.817	0.844
	1.105	1.233	1.383	1.458	1.396	1.227	1.039	0.922	0.719	0.669	0.766	0.824
	1.130	1.244	1.358	1.421	1.360	1.213	1.057	0.881	0.672	0.620	0.723	0.802
	1.134	1.236	1.343	1.376	1.311	1.190	1.052	0.843	0.637	0.583	0.686	0.777
	1.126	1.219	1.312	1.340	1.272	1.159	1.057	0.805	0.613	0.551	0.647	0.757
	1.107	1.198	1.280	1.270	1.239	1.123	1.037	0.769	0.587	0.529	0.618	0.726
	1.091	1.184	1.223	1.239	1.195	1.078	1.004	0.744	0.572	0.506	0.582	0.706
	1.053	1.108	1.118	1.075	1.092	1.022	0.987	0.722	0.574	0.478	0.557	0.661

Table 17: Relative reflectances for spruce trees, calculated using the mean of the tree top as reference. Column depict offset to Sun and rows correspond to relative heights of 2.5%...38.5% down from treetop.

Birch

	-90	-60	-30	0	30	60	90	-120	-150	180	150	120
RED	0.950	1.131	1.320	1.424	1.383	1.233	1.022	0.948	0.859	0.820	0.853	0.881
	0.991	1.191	1.379	1.464	1.407	1.278	1.088	0.882	0.775	0.738	0.783	0.837
	1.025	1.238	1.399	1.453	1.399	1.283	1.120	0.834	0.730	0.693	0.741	0.801
	1.070	1.266	1.394	1.423	1.362	1.267	1.138	0.804	0.702	0.658	0.703	0.766
	1.092	1.265	1.369	1.391	1.329	1.230	1.134	0.778	0.671	0.629	0.670	0.744
	1.125	1.258	1.362	1.371	1.295	1.179	1.139	0.739	0.642	0.603	0.639	0.723
	1.116	1.235	1.284	1.357	1.257	1.138	1.118	0.720	0.628	0.590	0.618	0.696
	1.139	1.192	1.254	1.259	1.191	1.112	1.110	0.705	0.607	0.572	0.595	0.687
	1.109	1.160	1.169	1.167	1.104	1.082	1.088	0.680	0.602	0.554	0.585	0.654
	1.101	1.054	1.052	0.979	0.937	0.959	0.995	0.674	0.591	0.560	0.572	0.640
GRN	0.948	1.122	1.305	1.413	1.367	1.214	1.015	0.953	0.858	0.825	0.857	0.879
	0.979	1.181	1.361	1.432	1.388	1.256	1.074	0.891	0.782	0.745	0.790	0.834
	1.017	1.219	1.371	1.422	1.368	1.259	1.102	0.848	0.740	0.704	0.750	0.800
	1.052	1.240	1.369	1.403	1.342	1.247	1.126	0.813	0.712	0.671	0.713	0.774
	1.073	1.246	1.342	1.370	1.310	1.211	1.117	0.785	0.680	0.644	0.683	0.752
	1.109	1.242	1.332	1.343	1.261	1.170	1.120	0.749	0.653	0.614	0.651	0.728
	1.087	1.218	1.265	1.339	1.218	1.116	1.101	0.732	0.633	0.597	0.630	0.706
	1.108	1.191	1.244	1.239	1.160	1.106	1.103	0.720	0.616	0.581	0.611	0.692
	1.087	1.140	1.145	1.156	1.086	1.063	1.091	0.691	0.607	0.563	0.600	0.656
	1.085	1.047	1.028	0.964	0.917	0.958	0.980	0.681	0.594	0.569	0.590	0.647
BLU	0.994	1.048	1.100	1.126	1.108	1.061	1.003	0.981	0.961	0.949	0.955	0.963
	1.005	1.063	1.113	1.134	1.115	1.070	1.017	0.958	0.932	0.916	0.925	0.943
	1.016	1.072	1.111	1.126	1.105	1.067	1.023	0.940	0.914	0.896	0.904	0.926
	1.025	1.073	1.104	1.111	1.093	1.060	1.027	0.926	0.898	0.879	0.889	0.910
	1.030	1.068	1.091	1.097	1.075	1.045	1.025	0.912	0.881	0.866	0.872	0.899
	1.037	1.061	1.082	1.081	1.057	1.031	1.024	0.897	0.868	0.849	0.856	0.885
	1.028	1.053	1.052	1.074	1.037	1.006	1.020	0.885	0.858	0.842	0.841	0.872
	1.030	1.038	1.043	1.033	1.010	1.002	1.013	0.879	0.847	0.828	0.833	0.861
	1.014	1.009	1.010	1.002	0.983	0.977	1.001	0.865	0.836	0.821	0.822	0.847
	0.998	0.972	0.958	0.936	0.927	0.940	0.965	0.860	0.827	0.810	0.815	0.838
NIR	0.953	1.135	1.354	1.483	1.441	1.260	1.019	1.022	0.945	0.897	0.891	0.879
	0.995	1.196	1.419	1.531	1.478	1.310	1.084	0.953	0.856	0.810	0.826	0.836
	1.041	1.243	1.433	1.516	1.456	1.318	1.123	0.892	0.792	0.752	0.778	0.800
	1.078	1.257	1.431	1.477	1.406	1.289	1.137	0.842	0.738	0.702	0.730	0.771
	1.102	1.250	1.393	1.425	1.347	1.240	1.133	0.789	0.680	0.649	0.689	0.743
	1.133	1.238	1.361	1.378	1.285	1.197	1.119	0.734	0.627	0.597	0.634	0.703
	1.121	1.209	1.259	1.328	1.202	1.112	1.097	0.688	0.591	0.553	0.587	0.666
	1.126	1.162	1.207	1.176	1.081	1.077	1.083	0.657	0.545	0.515	0.551	0.629
	1.102	1.078	1.078	1.034	0.983	0.985	1.032	0.616	0.516	0.480	0.515	0.586
	1.041	0.950	0.902	0.816	0.794	0.855	0.901	0.591	0.499	0.465	0.495	0.554

Table 18: Relative reflectances for birch trees, calculated using the mean of the tree top as reference. Column depict offset to Sun and rows correspond to relative heights of 2.5%...38.5% down from treetop.

5 Discussion and Conclusions

Automated tree species classification has been an active field of research in the past years in Scandinavia. The accuracy achieved at the moment still hasn't reached the needed level of 95% in Finland. In the same time as passive remote sensing sensors changed from analogue to digital, LiDAR had its breakthrough for forestry applications. With the new atmospherically correction, absolute calibration, and line-camera geometry, the ADS40 is able to regain ground in this area.

The possibility to calculate, for the first time ever, the values of at-target reflectances, could finally eliminate the influence of the medium between camera and target. It therefore reduces the effects of flying at different altitudes, as well as differences generated by collecting ground truth and image data from different regions. This would also be very beneficial in practical forest inventories and lead to improvements in cost-efficiency. First verifications showed that the accuracy (RMS) of the ATM data (1–4 km) was better than 10% for reference targets (Markelin et al., 2010), and the precision (SDEV) being better than 5% (Korpela et al., 2010). In this thesis, the effect of the atmospheric correction could be confirmed for the front-lit side of the trees. As expected, all slopes were dampened for the ATM image data. BLU showed to be affected most and reached R^2 -values up to 32.3%. While the front-lit side overall increased in radiance and reflectance values, the trend on the back-lit (shaded) side of the crown was exactly the opposite. The more the view zenith angle was increased, the intensities for the crown points were reduced. As these points were treated the same as in the sun-lit part of the crown (linear regression slope gets dampened), it is assumed, that this separation in different illumination classes is not contained in the used algorithm. This would also explain why the slope is never fully removed for sun-lit points and seems rather under corrected. As the influence of the atmosphere is usually modelled as an additional constant brightening effect, it would be interesting for further research, to investigate why this effect is not visible in self-shaded points. Especially because this part of the crown already showed to be a better predictor than the sun-lit area (Korpela, 2004; Korpela et al., 2010; Puttonen et al., 2009).

Changes caused by the atmospheric correction lowered when increasing the flying altitude to 4 km, which can be explained by the lower variation in the view zenith angle. On the other hand, for these flight lines, the plane flew directly over the trees of interest, thus having these in the middle of the image, instead of at the side as it was the case for the 30 cm-data.

While for these first experiments, the nadir view with a constant VA angle was used, the dependencies of VA were examined using the backwards looking data. To reduce the influence of the VZ angle, which is also present in these images, the atmospherically corrected versions were examined.

Although points on the sun-lit side of the tree mostly showed a linear trend with VA, the other half crown in diffuse light was found to be better fitting to the simple non-linear model chosen. Technically, the non-linear model was also better suited for the sun-lit side, but the run of the curve was usually almost identical to the linear regression. The different regression behaviour is another indication, that the two sides of a tree behave completely different. Maybe the direct sunlight gets scattered in multiple directions, therefore points appear at an almost equal brightness when changing the viewing direction.

Having analysed the different angles of the viewing geometry separately (as far as possible), in the third experiment, the reflectance variation of the whole crown surface was examined. Different

behaviours between tree species and bands became visible and leave room for further interpretation. While on the sun-lit side, points achieved 79.4%–153.1% of the mean reflectance at the top, the self-shaded part only reached values from 42.8% to 112.8%. BLU showed to be affected least (flat response), as the average standard deviation was only 3.5% compared to the other spectral bands, where the standard deviation was >10%. This can be explained by the BLU band having a higher ratio between hemispherical illumination and direct light compared to the other bands. As primarily scattered light defines the brightness of the tree crown in this spectrum, all crown points are affected evenly.

Visual representations of the relative crown values revealed that there are different pattern for each species (less in BLU). These different patterns could be caused by the different shape of the tree crowns as well as the branch/shoot level structures (clumping, shadow casting). Considering that every species reacts differently, a global atmospherical and BRDF correction might never be the perfect solution. But then, a segmented correction approach for each tree crown separately would quickly generate more disharmony in the image. Nevertheless, also taking into account the standard deviations for the reflectances at each crown position, the more stable points were determined. Particularly points which were positioned directly towards the sun ($pAngle=0$) or located at the opposite side ($pAngle=180$) had the lowest values for σ . At the side of the trees, the relative reflectances varied more. A reason for this might be that when seeing a tree from the side, a mixture of sun-lit branch tips and parts of branches, which are shaded by others parts of the tree, are visible. Mainly the complex illumination inside a crown is visible, while at a $pAngle$ -value of 0 or 180, either the area is either well sun-lit or shaded.

Knowing where the illumination of crown points is most stable, might raise the question, if a specific sampling in this area wouldn't be better suited. Above all, because modelling a crown surface, which in nature does not really exist, introduces additional errors. Another idea would also be the direct use of the LiDAR position for sampling, instead of an artificially created surface point set. This might lead to better results, as the offset between crown and envelope would not exist anymore. The question then would be, if the algorithm, which samples the image strips, fulfils the required accuracy and how to assign LiDAR points to trees. As LiDAR hits might as well also be inside the crown, the extraction of the corresponding spectral information could be challenging, because of the different observation geometries of images and LiDAR.

In this thesis, multicollinearities between variables were tried to be avoided by choosing the correspondent view (N00A, B16A) and the image version (ASR, ATM). As such unwanted dependencies can also be caused by natural factors (i.e. age, healthiness, site fertility, stand density/treatment history) further investigation would be necessary. Especially in managed forests, these factors are not only affecting single trees, but more whole stands of trees (as they are planted at the same time and same place). Already the effect of neighbouring trees showed to increase reflectances up to 33% (for SS points in NIR) (Korpela et al., 2010).

Limited by the defined time frame, only a part of the experiments possible with this data could be performed, thus leaving room for further research. Analyses were done on flight strips with an altitude of 2 km or higher. Even though high resolution data with 10 cm GSD would provide structural features, which could be used to extract additional features (Erikson, 2004), such imagery always comes with a higher price tag. Also, the algorithm for correcting the BRDF effects was not applied. Korpela et al. (2010) showed that the BRDF algorithm is especially effective in strips flown

perpendicular to the sun, as these are affected by a strong cross track gradient. However, as the anisotropy varies between species, one correction is insufficient.

A simplification chosen was the assumption that the solar illumination does not change during the acquisition of a flight line. While this generalisation together with the design of the camera reduced the complexity of the illumination geometry, it hindered the analysis of the SA and SZ angles. To obtain a higher variation in all of the four main angles, a different flight plan would be needed. Comparing observations from strips with altered flying direction would enable a verification of the present results. Additionally, this might also help to detect multicollinearities in the ground reference data. More variation in the heading for each flight line would as well enable a more detailed analysis of the crown.

As the collected data is based on crown point features, common classification algorithms used for the determination of the tree species (being a tree feature) might not be applicable in this situation. A way of combining the information of all crown points for a tree is needed. Furthermore, first classification test revealed, that R and SAS (version 9.2) are struggling to handle a data set with 15'197 x 121 observations. Therefore an approach where the information of all observations for each tree is merged to a few attributes might be preferred to just classifying all crown points separately (Korpela et al., 2010). Whilst already combining information from several crown points, maybe adding information from the second view increases the predicting stability of this attribute.

An example of such a method which combines the information of all crown points would be to treat the information gained in experiment three as templates (Table 16-Table 18). For each tree, the relative values of the crown point to the top could then be calculated and compared to its reference in the template. Using the residuals, an indicator for the fit (i.e. RMSE) to each different species-template can then be calculated. This approach would use all available crown points to predict the tree species, and even provides a quality measure. To improve the accuracy, maybe only the points in well-defined areas ($\rho\text{Angle}=0/180$) should be used as a template. Because of occlusions, the templates would be sparse.

Overall, the ADS40 showed to be well suited for such an analysis. The data indicated that the combination between LiDAR point information together with digital imagery worked seamlessly. The effects of the reflectance anisotropy can easily be observed down to the very last crown position at the base of the tree crown. While the design of the camera simplifies the modelling of the anisotropy effects, only additional research with image data showing more variation in the flying direction will verify the present results.

6 References

- Albertz, J. and Wiggerhagen, M. (2009) *Guide for Photogrammetry and Remote Sensing*, 5th edition, Heidelberg: Herbert Wichmann Verlag.
- Beisl, U. (2006) 'Absolute Spectroradiometric Calibration of the ADS40 Sensor', IAPRS Vol. 36, Part 1B, Paris, France.
- Beisl, U., Telaar, J. and v. Schönemark, M. (2008) 'Atmospheric Correction, Reflectance Calibration and BRDF Correction for ADS40 Image Data', Beijing, China, 7-12.
- Beisl, U. and Woodhouse, N. (2008) 'Correction Of Atmospheric and Bidirectional Effects in Multispectral ADS40 Images for Mapping Purposes', ISPRS Commission VII, WG VII/1.
- Brandtberg, T. (1999) 'Automatic individual tree based analysis of high spatial resolution aerial images on naturally regenerated boreal forests', *Canadian Journal of Forest Research*, pp. 1464-1478.
- Brandtberg, T. (2002) 'Individual tree-based species classification in high spatial resolution aerial images of forests using fuzzy sets', *FUZZY sets and systems*, pp. 371-387.
- Casella, V., Franzini, M., Banchini, G. and Gentili, G. (2008) 'Initial evaluation of the second-generation Leica ADS40 camera', Beijing, China.
- Chavez, P.S. (1988) 'An Improved Dark-Object Subtraction Technique for Atmospheric Scattering Correction of Multispectral Data', *Remote Sensing of Environment*, pp. 459-479.
- Cramer, M., Stallmann, D. and Haala, N. (2000) 'Direct georeferencing using GPS/inertial exterior orientations for photogrammetric applications', IAPRS, Amsterdam, 198-205.
- Deering, D.W., Eck, T.F. and Banerjee, B. (1999) 'Characterization of the reflectance anisotropy of three boreal forest canopies in spring-summer', *Remote Sensing of Environment*, pp. 205-229.
- Deering, D.W., Middleton, E.M. and Eck, T.F. (1994) 'Reflectance Anisotropy for a Spruce-Hemlock Forest Canopy', *Remote Sensing of Environment*, pp. 242-260.
- Erikson, M. (2004) 'Species classification of individually segmented tree crowns in high-resolution aerial images using radiometric and morphologic image measures', *Remote Sensing of Environment*, pp. 469-477.
- Fraser, R.S., Ferrare, R.A., Kaufman, Y.J., Markham, B.L. and Mattoo, S. (1992) 'Algorithm for atmospheric corrections of aircraft and satellite imagery', *International Journal of Remote Sensing*, pp. 541-557.
- Fricker, P. (2007) 'Raising the bar for multi-band, high-resolution airborne imagery', Photogrammetric Week '07, Heidelberg, Germany, 71-79.
- Haara, A. and Haarala, M. (2002) 'Tree species classification using semi-automatic delineation of trees on aerial images', *Scandinavian Journal of Forest Research*, pp. 556-565.
- Heikkinen, V., Korpela, I., Tokola, T., Honkavaara, E. and Parkkinen, J. (2010) 'An SVM classification of tree species radiometric signatures based on the Leica ADS40 sensor'.

- Holmgren, J., Persson, Å. and Söderman, U. (2008) 'Species identification of individual trees by combining high resolution LiDAR data with multi-spectral images', *International Journal of Remote Sensing*, pp. 1537-1552.
- Hyyppä, J., Hyyppä, H., Leckie, D., Gougeon, F., Yu, X. and Maltamo, M. (2008) 'Review of methods of small-footprint airborne laser scanning for extracting forest inventory data in boreal forests', *International Journal of Remote Sensing*, pp. 1339-1366.
- Hyyppä, J. and Inkinen, M. (1999) 'Detecting and Estimating Attributes for Single Trees Using Laser Scanner', *The Photogrammetric Journal of Finland* 16, pp. 27-42.
- Kaufman, Y.J. and Sendra, C. (1988) 'Algorithm for automatic atmospheric corrections to visible and near-IR satellite imagery', *International Journal of Remote Sensing*, pp. 1357-1381.
- Korpela, I. (2004) *Individual Tree Measurements by Means of Digital Aerial Photogrammetry*, Sylva Fennica Monographs.
- Korpela, I. (2007) '3D Treetop Positioning by Multiple Image Matching of Aerial Images in a 3D Search Volume Bounded By LiDAR Surface Models', *Proceedings Photogrammetric Computer Vision 2006*, Bonn, 35-44.
- Korpela, I. (2008) 'Mapping of understory lichens with airborne discrete-return LiDAR data', *Remote Sensing of Environment*, pp. 3891-3897.
- Korpela, I., Heikkinen, V., Honkavaara, E., Rohrbach, F. and Tokola, T. (2010) 'Variation and Anisotropy of Reflectance of Forest Trees in Radiometrically Calibrated Airborne Line Sensor Images - Implications to Species Classification'.
- Korpela, I., Orka, H.O., Maltamo, M., Heikkinen, V. and Tokola, T. (2010) 'Tree species classification using airborne LiDAR - effects of stand and tree parameters, downsizing of training set, intensity normalization and sensor type', *Silva Fennica* 44.
- Korpela, I. and Tokola, T. (2006) 'Potential of Aerial Image-Based Monoscopic and Multiview Single-Tree Forest Inventory: A Simulation Approach', *Forest Science*, pp. 136-147.
- Korpela, I., Tuomola, T., Tokola, T. and Dahlin, B. (2008) 'Appraisal of seedling stand vegetation with airborne imagery and discrete-return LiDAR - an exploratory analysis', *Silva Fennica*, pp. 753-772.
- Larsen, M. (2007) 'Single tree species classification with a hypothetical multi-spectral satellite', *Remote Sensing of Environment*, pp. 523-532.
- Leckie, D.G., Gougeon, F.A., Walsworth, N. and Paradine, D. (2003) 'Stand delineation and composition estimation using semi-automated individual tree crown analysis', *Remote Sensing of Environment*, pp. 355-369.
- Li, X. and Strahler, A.H. (1986) 'Geometric-Optical Bidirectional Reflectance Modeling of a Conifer Forest Canopy', *IEEE Transactions on Geoscience and Remote Sensing*, 6 November.
- Markelin, L., Honkavaara, E., Beisl, U. and Korpela, I. (2010) 'Validation of the Leica ADS40 Radiometric Processing Chain', *ISPRS Commission VII, WG VII/1*.

- Meyer, P., Staenz, K. and Itten, K. (1996) 'Semi-automated procedures for tree species identification in high spatial resolution data from digitized colour infrared-aerial photography', *ISPRS Journal of Photogrammetry & Remote Sensing*, pp. 155-165.
- Næsset, E. (1997) 'Estimating Timber Volume of Forest Stands Using Airborne Laser Scanner Data', *Remote Sensing of Environment*, August, pp. 246-253.
- Næsset, E. (2002) 'Predicting forest stand characteristics with airborne scanning laser using a practical two-stage procedure and field data', *Remote Sensing of Environment*, pp. 88-99.
- Nilson, T. and Peterson, U. (1991) 'A Forest canopy reflectance model and a test case', *Remote Sensing of Environment*, pp. 131-142.
- Packalén, P., Suvanto, A. and Maltamo, M. (2009) 'A Two Stage Method to Estimate Species-specific Growing Stock', *Photogrammetric Engineering & Remote Sensing*.
- Puttonen, E., Litkey, P. and Hyypä, J. (2009) 'Usability of a sunlit-shaded area separation in individual tree species classification', Proc. ISPRS Workshop Laserscanning 2009, Paris, France, 311-316.
- Rautiainen, M., Lang, M., Möttö, M., Andres, K., Nilson, T., Kuusk, J. and Lück, T. (2008) 'Multi-angular reflectance properties of a hemiboreal forest: An analysis using CHRIS PROBA data', *Remote Sensing of Environment*, pp. 2627-2642.
- Rautiainen, M. and Stenberg, P. (2005) 'Application of photon recollision probability in coniferous canopy', *Remote Sensing of Environment*, pp. 98-107.
- Rautiainen, M., Stenberg, P., Nilson, T. and Kuusk, A. (2004) 'The effect of crown shape on the reflectance of coniferous stands', *Remote Sensing of Environment*, pp. 41-52.
- Rohde, W.G. and Olson, C.E. (1972) 'Multispectral Sensing of Forest Tree Species', *Photogrammetric Engineering*, March, pp. 1209-1215.
- Sandmeier, S. and Deering, D.W. (1999) 'Structural analysis and classification of boreal forests using airborne hyperspectral BRDF data from ASAS', *Remote Sensing of Environment*, pp. 281-295.
- Schaepman-Strub, G., Schaepman, M.E., Painter, T.H., Dangel, S. and Martonchik, J.V. (2006) 'Reflectance quantities in optical remote sensing - definitions and case studies', *Remote Sensing of Environment*, 4 March.
- Song, J., Lu, D. and Wesely, M.L. (2003) 'A Simplified Atmospheric Correction Procedure for the Normalized Difference Vegetation Index', *Photogrammetric Engineering & Remote Sensing*, May, pp. 521-528.
- Tomppo, E., Henttonen, H. and Tuomainen, T. (2001) *Valtakunnan metsien 8. inventoinnin menetelmä ja tulokset metsäkeskuksittain Pohjois-Suomessa 1992-94 sekä tulokset Etelä-Suomessa 1986-92 ja koko maassa 1986-94*, Metsätieteen aikakauskirja IB/2001.
- Walthall, C.L. (1997) 'A Study of Reflectance Anisotropy and Canopy Structure Using a Simple Empirical Model', *Remote Sensing of Environment*, pp. 118-128.